nature communications

Article

https://doi.org/10.1038/s41467-025-59650-0

Chemotactic Zn micromotor for treatment of high blood ammonia-associated hepatic encephalopathy

Received: 18 August 2024

Accepted: 28 April 2025

Ye Feng[1], Chao Gao[1], Xiuyun Peng[2], Bin Chen[1], Miaomiao Ding[1], Dailing Du[1], Jinghui Rong[1], Qi Lv[1], Daniela A. Wilson[3], Yingfeng Tu[4] & Fei Peng[1] ✉

Hepatic fibrosis involves hepatocyte damage, causing blood ammonia accumulation, which exacerbates liver pathology and crosses the blood-brain barrier, inducing hepatic encephalopathy. It is meaningful to construct a therapeutic platform for targeted ammonia clearance. In this work, a biocompatible water-powered Zn micromotor is constructed as an ammonia chemotaxis platform, which can be actuated by the water splitting reaction and the self-generated Zn^{2+} gradient. It can propel towards $NH_3{\cdot}H_2O$ source through the formation of complex ions $[Zn(NH_3)_1](OH)^+$ and $[Zn(NH_3)_2](OH)^+$, representing a generalizable chemotaxis strategy via coordination reaction. In vivo, biomimetic collective behavior allows precise navigation and reduction of the intrahepatic ammonia level, reshaping the pathological microenvironment. This mechanism, operating in a green, zero-waste manner, facilitates integration of these micromotors into the domain of biological regulation. Such environment environment-adaptive platform is favorable for targeted treatment of hepatic fibrosis and hepatic encephalopathy caused by hyperammonemia, which is expected to provide inspiration for future personalized and precision medicine.

Ammonia is a natural endogenous molecule[1]. In vivo, blood ammonia primarily originates from the catabolism of amino acids and proteins by bacteria in the gut, hydrolysis of urea, and deamidation of amino acids in liver[2]. The produced ammonia is typically metabolized in the liver through catalysis of low-toxic glutamine from NH_4^+ by glutamine synthetase[3] or ammonia conversion into urea[4–6]. Under normal conditions, the liver maintains blood ammonia (lower than 50 µM in serum) at a low level of dynamic equilibrium. However, upon the metabolic function of hepatocytes decreases, excessive accumulation of ammonia in the liver is resulted, along with a rise in blood ammonia levels[7]. Ammonia accumulation results in inflammatory necrosis of liver cells, even liver fibrosis and cirrhosis[8,9]. Hyperammonemia can further lead to hepatic encephalopathy[10–13], with clinical manifestations including behavioral disorders, and even coma[14,15]. Ammonia permeates the blood-brain barrier predominantly via passive diffusion in its neutral form (NH_3), while the ammonium ion (NH_4^+) traverses to a lesser extent through potassium transporter-mediated mechanisms[16–18]. Astrocytes are the only brain cells capable of metabolizing ammonia; however, excessive ammonia causes astrocyte edema[19–22], which inhibits the possibility of neuronal repair, causing irreversible brain damage[23,24]. Therefore, targeted ammonia clearance is meaningful for the hepatic encephalopathy therapy.

In nature, a wide variety of chemical attractants exist[25]. These chemical gradients can attract or repel corresponding organisms. In the macroscopic world, insects locate food by chemotaxis to food and are attracted to pheromones released by the opposite sex for mating[26].

---

[1]School of Materials Science and Engineering, Sun Yat-sen University, Guangzhou, China. [2]Key Laboratory of Joint Diagnosis and Treatment of Chronic Liver Disease and Liver Cancer of Lishui, Lishui People's Hospital, Lishui, China. [3]Institute for Molecules and Materials, Radboud University, Nijmegen, The Netherlands. [4]Guangdong Provincial Key Laboratory of New Drug Screening, School of Pharmaceutical Sciences, Southern Medical University, Guangzhou, China.
✉e-mail: pengf26@mail.sysu.edu.cn

Similarly, inflamed tissues release specific chemicals (chemokines) that guide neutrophils along the concentration gradient[27–29]. Inspired by the chemotactic behavior of organisms in nature, researchers engineered artificial micro/nanomotors capable of chemotactic movement mimicking microscopic organisms[30–32]. These synthetic micro/nanomotors autonomously move by converting chemical[33,34], acoustic[35], optical[36], electrical[37] and magnetic[38] energy into mechanical energy, and follow the environmental cues towards areas of higher chemical fuel concentration[39,40], which holds promise for precision medicine[41].

Chemotaxis can arise from the thermodynamic driving force that lowers chemical potential with favorable substrate binding, with enzyme-substrate systems being described more often. In addition, researchers proposed the ZnO nanorod sulfonated PS microbead system. Through the ion exchange reaction, collective behavior and mobility is resulted[42]. Here, we propose a water-driven Zn micromotor (Fig. 1a) via the reaction of Zn with H^+ in water. The Zn micromotors can demonstrate chemotactic migration towards $NH_3 \cdot H_2O$ (Fig. 1b) via the coordination between Zn and $NH_3 \cdot H_2O$. We demonstrate that the ammonia concentration gradient generated by both static and dynamic flow chemotaxis device promotes the collective chemotaxis of Zn micromotors. We present a kinetic system capable of autonomous chemotaxis through coordination. For hepatic encephalopathy caused by excessive blood ammonia resulting from liver injury, the central problem is to reduce the concentration of ammonia in the body. The ammonia absorption into blood occurs in the colon and the main metabolizing organ is liver, both of which are high concentrated sites of blood ammonia[6]. The chemotactic migration of Zn micromotors towards ammonia

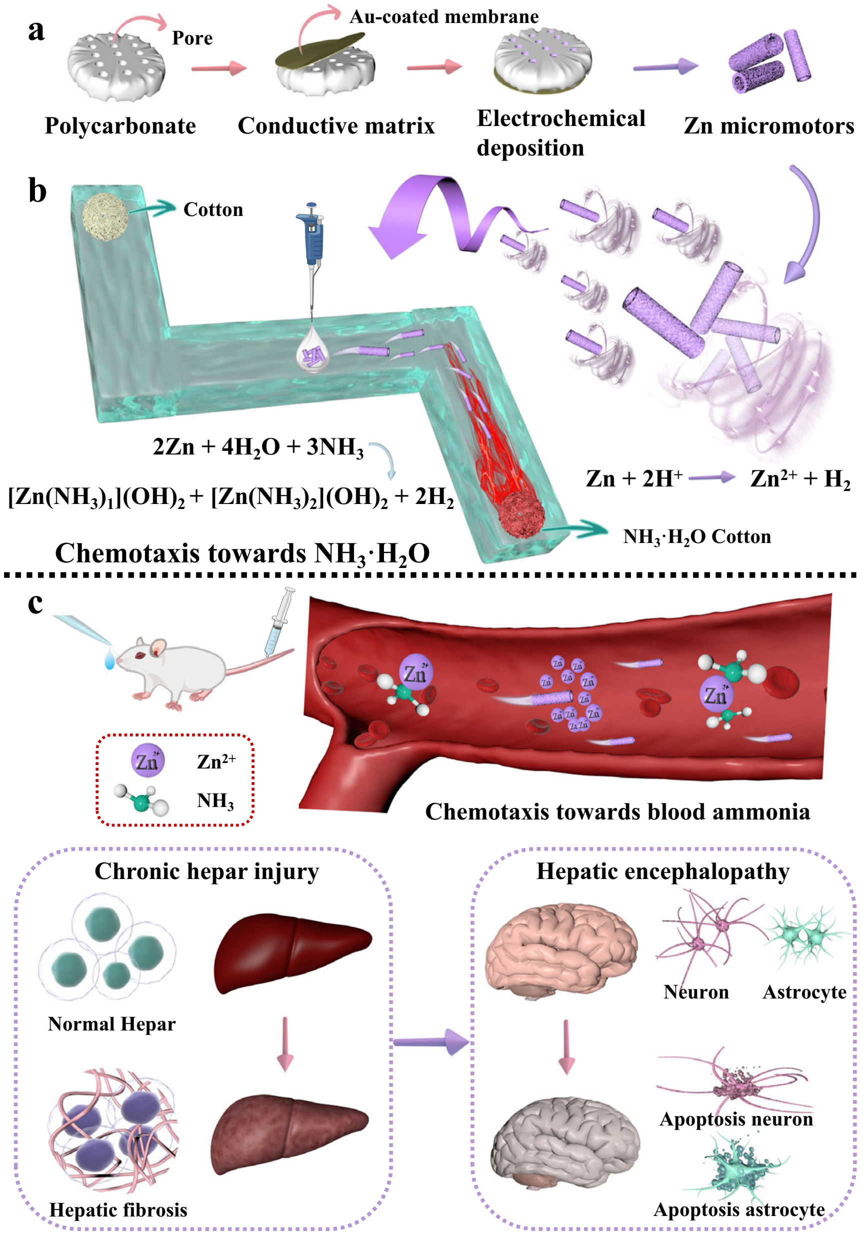

Fig. 1 | Schematic diagram showing the construction of Zn micromotors, chemotactic migration towards $NH_3 \cdot H_2O$, and targeting to promote ammonia metabolism in vivo. a Manufacture of Zn micromotors by electrodeposition using the PC membrane template method. **b** Chemotactic migration evaluation of Zn micromotors towards ammonia. In a Z-shaped glass channel, ammonia is added at one end of the channel, and the diffusion of ammonia creates a concentration gradient, guiding the Zn micromotors to migrate towards ammonia ammonia-enriched region. **c** Zn micromotors assist ammonia metabolism and improve hepatic fibrosis. Micromotors further reduce brain permeable ammonia, slow down neuronal death, and improve hepatic encephalopathy. Some elements in this figure are reproduced from the MATRIX resource library, copyright Hangzhou SPHERE Tech. Ltd.

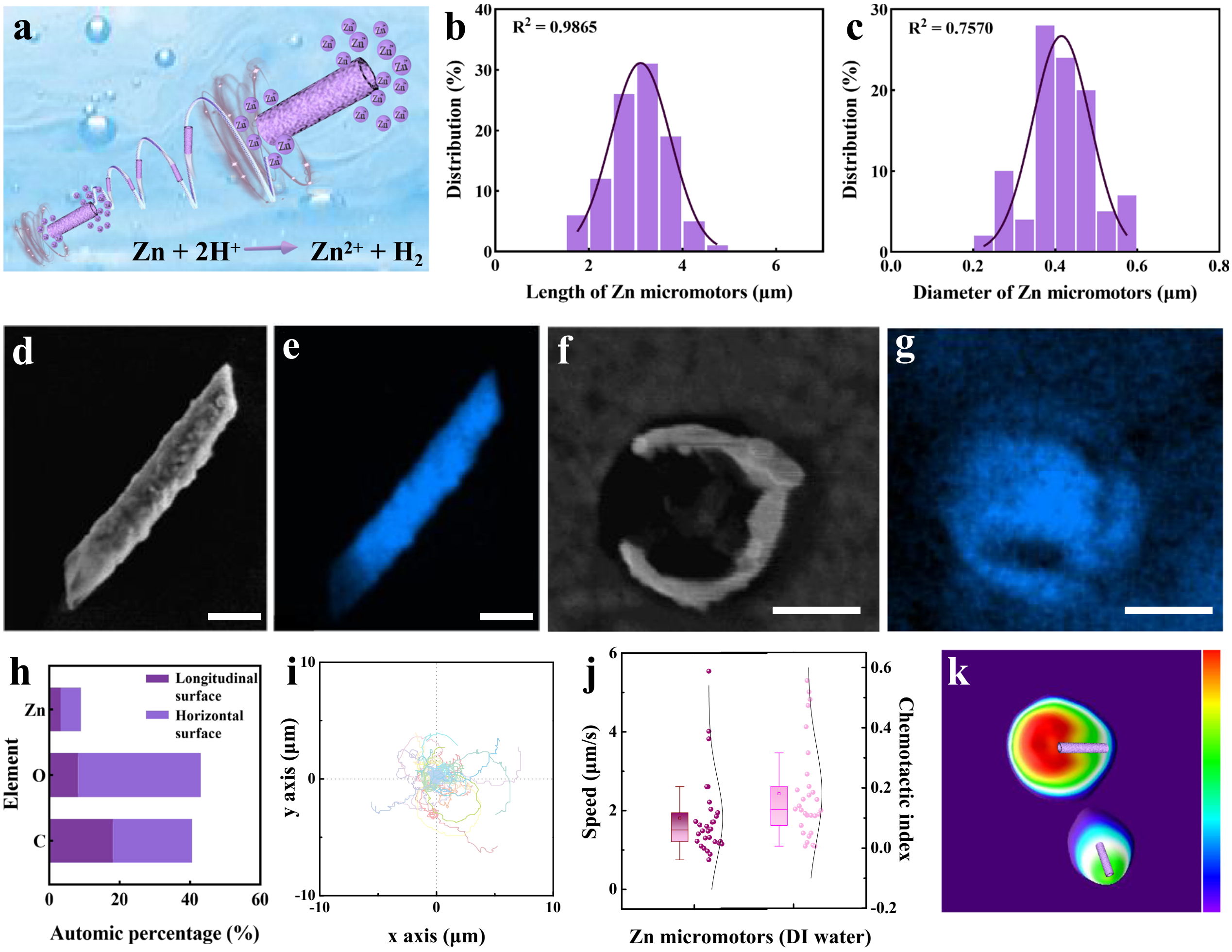

Fig. 2 | Characterization and motion performance of Zn micromotors. a Self-propulsion mechanism of Zn micromotors in water. **b** Length distribution of Zn micromotors. **c** Diameter distribution of Zn micromotors. **d** SEM image of a single Zn micromotor. Scale bar: 600 nm. **e** Elemental mapping of a Zn micromotor. Scale bar: 600 nm. **f** SEM image of a single Zn micromotor cross section. Scale bar: 200 nm. **g** Elemental mapping of a Zn micromotor cross section. Scale bar: 200 nm. **h** Element composition corresponding to Zn micromotor (on silicon substrate). **i** Normalized moving trajectories of the Zn micromotors within 10 s (time interval = 100 ms) (*n* = 30 independent samples). **j** Statistics of speed and directionality of Zn micromotors in water (*n* = 30 independent samples). Results were shown as box plots (The box represents the interquartile range (IQR), with the middle line indicating the median, the top and bottom edges of the box show the upper (Q3) and lower (Q1) quartiles respectively, while the whiskers extend to the maximum and minimum values of the dataset.) **k** Fluorescence intensity analysis of Zn^{2+} around the Zn micromotors. In d-g, the full name of Zn is Zinc. In d-h and k, the experiment was repeated independently three times with similar results, and a representative result is shown. Data in **b**, **c**, **i** and **j** represented as mean values ± S.D. Source data are provided as a Source Data file. Some elements in this figure are reproduced from the MATRIX resource library, copyright Hangzhou SPHERE Tech. Ltd.

could be directed to the colon and liver. Upon arrival, local ammonia is trapped through a coordination reaction, promoting local ammonia metabolism. The reduction of ammonia concentration in the body is found to improve hepatic fibrosis/hepatic encephalopathy (Fig. 1c). This autonomous chemotaxis platform provides a direction for the field of precision medicine.

Results

Morphology characterization and motion mechanism of Zn micromotors

The template approach was utilized to prepare Zn micromotors (Fig. 1a), with a polycarbonate membrane (average pore size of about 400 nm) to control the size and morphology of the micromotors. Initially, a gold layer approximately 100 nm thick was sputtered on one side of the polycarbonate film to enhance the conductivity of template. Then, the gold-plated PC film was used as the working electrode to deposit a Zn tube (three-electrode method). Organic reagent was then employed to dissolve the PC film, and the harvested Zn micromotors were dispersed in deionized water (DI) (Fig. 2a). Following the preparation, the morphology of the Zn micromotors were characterized by scanning electron microscopy (SEM) (Supplementary Fig. 1). The length and diameter of the Zn micromotors were determined using ImageJ software, with a length of 3.07 ± 0.65 μm (Fig. 2b) and a diameter of 0.41 ± 0.08 μm (Fig. 2c). The quantitative distribution of Zn elements was analyzed using energy dispersive X-ray spectroscopy (EDX) (Supplementary Fig. 2). As shown in Fig. 2d and e, the wall of the Zn micromotor was thicker at one end (bottom) and thinner at the other end (top) due to the gradual deposition from bottom to top inside the template by controlling the deposition time. The distribution of Zn further showed that there is a Zinc content difference between the two ends. A part of the electrodeposited PC film was captured, and it was observed by SEM that hollow tubular structure was formed along the template wall (Supplementary Fig. 3). A Horizontal surface of Zn micromotors was enlarged (Fig. 2f), and the distribution of Zn elements was analyzed by EDX (Fig. 2g, Supplementary Fig. 4). As shown in Fig. 2h, the Zn content was quantitatively analyzed on the horizontal surface (Zinc content 5.79%) and longitudinal planes (Zinc content 3.20%).

Zn micromotors were harvested from the template and dispersed in water. The micromotors were observed through a microscope to investigate the mechanism of motion[43]. It was found that the Zn micromotors performed self-propelled motion in water in a circular manner. Its autonomous motion was primarily due to the reaction between Zn and H^+ in water, with the reaction formula (Fig. 2a) :

$$Zn + 2H^+ \rightarrow Zn^{2+} + H_2$$

Since Zn was gradually deposited along the membrane pores from the bottom of the PC film template (near the Au end) upwards during the electrochemical deposition, the Zn micromotor is of an asymmetric structure, being thicker at one end (near the gold layer end) and thinner at the other end (far from the gold layer end). As the reaction progressed, the Zn^{2+} accumulates higher than that at the thicker end of the micromotor wall. Therefore, it created a Zn^{2+} concentration gradient around the Zn micromotor, resulting in a self-generated electric field. The direction of the electric field was from the thin end to the thick end, driving the Zn micromotor towards the higher potential (thinner micromotor wall). The moving trajectories of the Zn micromotors over time were plotted as shown in Fig. 2i, Supplementary Fig. 5 and Supplementary Movie 1. The average speed (1.78 ± 1.02 µm/s) and directionality (0.19) of the micromotors were calculated (Fig. 2j, Supplementary Table 1). Spiral forward motion was the typical moving pattern of Zn micromotors. No bubbles were produced during the movement. The moving mechanism of the Zn micromotor was further demonstrated with a Zn^{2+} fluorescent probe (Zinquin), which can combine with Zn^{2+} to produce fluorescent signal (Supplementary Fig. 6). As shown in the Fig. 2k, there was fluorescence aggregation around the Zn micromotor, and the fluorescence intensity was positively correlated with the concentration of Zn^{2+}. The fluorescence intensity showed a gradual decreasing trend from one end of the Zn micromotor to the other end, which proved that there was indeed a Zn^{2+} concentration gradient field around the micromotors.

Collective chemotaxis dynamics of Zn micromotors

The movement mechanism of single Zn micromotor has already been demonstrated. While previous micromotors can move autonomously, they often exhibit poor directionality and lack the capability to perform complex tasks. However, it has been observed that cells and microorganisms in nature can respond to chemical attractants, leading to collective chemotactic behavior. Inspired by this natural phenomenon, we designed a biomimetic chemotaxis system, Zn micromotors for collective migration towards ammonia enriched areas. Without applying additional external field, the directional navigation of the Zn micromotors is guided through the concentration gradient of ammonia.

Firstly, cotton soaked with either $NH_3{\cdot}H_2O$ or water was placed on the left side inside a Petri dish, and Zn micromotors were introduced onto the right side. The trajectories of the micromotors were observed and recorded (Fig. 3a). When cotton was soaked with 150 µM $NH_3{\cdot}H_2O$ (10 µL), the movement of the Zn micromotors was tracked (Supplementary Movie 2). As shown in Fig. 3b and c, the Zn micromotors showed a tendency to move directionally towards the left where the ammonia was located, with an average speed of 1.12 ± 0.73 µm/s and a directionality of 0.24 (Supplementary Table 2) When cotton was soaked with 1500 µM $NH_3{\cdot}H_2O$, the moving process (Supplementary Movie 3) of the Zn micromotors was recorded, and the velocity increased to 1.74 ± 1.33 µm/s, showing directional movement towards the $NH_3{\cdot}H_2O$ (Fig. 3d, e), with a directivity of 0.21 (Supplementary Table 2). When cotton was soaked in water (Supplementary Movie 4), the statistical analysis of the motion trajectories and direction data was shown in Supplementary Figs. 7, 8. In this case, Zn micromotors lacked directional movement, with an average movement speed of 0.87 ± 0.60 µm/s and directionality of 0.12 (Supplementary Table 2).

The response of Zn micromotors to different chemical attractant (150 µM $NH_3{\cdot}H_2O$, 1500 µM $NH_3{\cdot}H_2O$) (Fig. 3f) was statistically analyzed. Compared with that in water, the speed of Zn micromotors increased by 28.74% in the 150 µM $NH_3{\cdot}H_2O$ attractant system and by 100.00% in the 1500 µM $NH_3{\cdot}H_2O$ attractant system. Similarly, the chemotaxis directionality (Fig. 3g) of the Zn micromotors increased by 100.00% in the 150 µM $NH_3{\cdot}H_2O$ attractant system and 75.00% in the 1500 µM $NH_3{\cdot}H_2O$ attractant system, compared with in water. Based on these experimental results, it was determined that the Zn micromotors could demonstrate collective behavior of chemotaxis toward $NH_3{\cdot}H_2O$.

In order to evaluate the behavior of Zn micromotors in a dynamic environment, chemotaxis of Zn micromotors was continued to be validated in microfluidic channels. As shown in Fig. 3h, the three-inlet microfluidic channel provides a dynamic flow environment. A flow rate of 0.2 mL/h remained unchanged throughout the flow experiment. $NH_3{\cdot}H_2O$ was introduced into inlet A, Zn micromotors into inlet B, and H_2O into inlet C. When the solution of each channel reached the steady-state profile, the motion trajectory of Zn micromotors was observed and recorded (Fig. 3i). For channel A ($NH_3{\cdot}H_2O$) and channel B (Zn micromotors), the results were shown in Fig. 3j and Supplementary Movie 5a, and the moving trajectory of Zn micromotors shifted towards channel A. The offset angle was (33.73 ± 10.88)° (Fig. 3k). For channel C (H_2O) and channel B (Zn micromotors), the trajectory of Zn micromotors did not shift significantly (Fig. 3l and Supplementary Movie 5b), and the offset angle was (7.65 ± 3.93)° (Fig. 3m). The above experimental results proved that Zn micromotors can move towards ammonia chemotaxis in the flowing fluid environment.

Collective chemotaxis of Zn micromotors in glass channels

To further evaluate the $NH_3{\cdot}H_2O$ chemotaxis behavior of Zn micromotors, we designed a Z-shaped glass channel for evaluating chemotaxis over longer distances, as shown in Fig. 4a, and the specific parameters were shown in Supplementary Fig. 9. We checked the possible external interference of the channel. First, the Z-shaped glass channel filled with water was thermo-imaged at room temperature, and after 1 h of monitoring, as shown in Supplementary Fig. 10, the temperature is uniform in all locations of the channel, and there are no temperature differences. Thus, the influence of temperature on the movement of Zn micromotor can be ruled out. Then, phenolphthalein indicator was added to the channel, and cotton soaked in $NH_3{\cdot}H_2O$ (10 µL) was positioned in chamber B. $NH_3{\cdot}H_2O$ diffusion was observed (Supplementary Fig. 11. and Supplementary Movie 6). It was found that $NH_3{\cdot}H_2O$ diffused slowly through the channel in a steady unidirectional flow, which created an ammonia concentration gradient. It did not present turbulence, vortex and other flow disturbances. Thus, the influence of fluid dynamics on the movement of Zn micromotors can be ruled out. $NH_3{\cdot}H_2O$ diffused slowly in the channel to form an ammonia concentration gradient. The glass channel was filled with water, and the $NH_3{\cdot}H_2O$ concentration in chamber B was 150 mM (10 µL). A 10 µL aliquot of Zn micromotors dispersed in water was placed at position C in the middle of the channel (Fig. 4a), and the two positions of the left turn (point D) and the right turn (point E) were selected as observation points. The movement of the Zn micromotors at these two positions was recorded (Supplementary Movies 7 and 8). The moving trajectories of the Zn micromotors at the point D (in the direction of water attractant) were normalized (Supplementary Fig. 12), and the chemotaxis data were statistically analyzed (Supplementary Fig. 13). The results showed that the Zn micromotors lacked directional movement, with an average motion speed of 0.04 ± 0.02 µm/s and directionality 0.02 (Supplementary Table 3). Figure 4b showed the trajectories of the Zn micromotors at point E (in the direction of the ammonia attractant). According to statistical analysis, the average velocity of the Zn micromotors increased to 0.14 ± 0.02

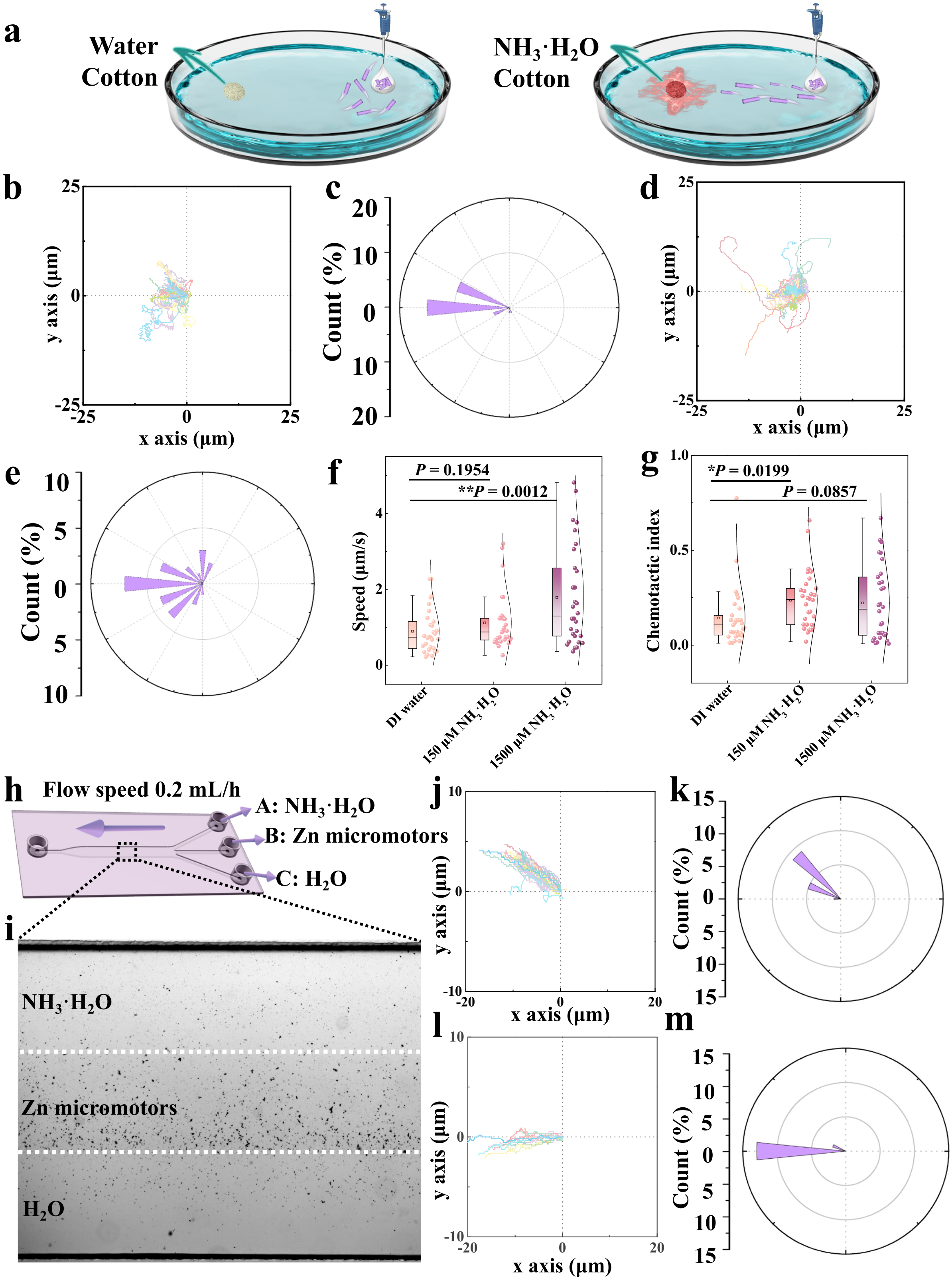

μm/s and the directionality increased to 0.06 (Fig. 4c, Supplementary Table 3). The Zn micromotors showed directional motion. Compared with the point D, the average movement speed of the point E increased by 250.00%, and the directionality increased by 200.00% (Fig. 4d). Then, the long-term clustering of Zn micromotors was observed at chamber A (water soaked cotton) and chamber B ($NH_3·H_2O$ soaked cotton), respectively. As shown in Supplementary Fig. 14a, there was no aggregation of Zn micromotors near the chamber A (water soaked cotton) within 40 min. As shown in Supplementary Fig. 14b, at 10 min, particles gradually moved to the source of $NH_3·H_2O$ (chamber B). The amount of Zn micromotors gathered at the $NH_3·H_2O$ source gradually increased with extended time. It showed that Zn micromotors had the ability to collectively move towards high-concentration ammonia. Next, a series of control experiments were set up. Firstly, both ends

Fig. 3 | Chemotaxis kinetics evaluation of Zn micromotors. a Schematic diagram of chemotactic movement of Zn micromotors in Petri dish. **b** Normalized movement trajectories and **c** Corresponding statistics of the direction distribution of Zn micromotor movement (*n* = 30 independent samples) were recorded when cotton soaked with 150 μM $NH_3{\cdot}H_2O$ (10 μL) was added to the left side. **d** Normalized movement trajectories and **e** Corresponding statistics of the distribution of the direction distribution of Zn micromotors (*n* = 30 independent samples) were recorded when cotton soaked with 1500 μM $NH_3{\cdot}H_2O$ (10 μL) was added to the left side. **f** The movement speed of each group was compared (*n* = 30 independent samples). **g** The Chemotactic Index (CI) values of each group were compared (*n* = 30 independent samples). Results in **f**, **g** were shown as box plots (The box represents the interquartile range (IQR), with the middle line indicating the median, the top and bottom edges of the box show the upper (Q3) and lower (Q1) quartiles respectively, while the whiskers extend to the maximum and minimum values of the dataset.) DI Water is control group. **h** Schematic of chemotaxis of Zn micromotors in a three-inlet microfluidic channel. $NH_3{\cdot}H_2O$ was introduced via channel A, Zn micromotors was introduced via channel B, and H_2O is introduced via channel C. **i** The observation recording site when the solution of each channel reached the steady-state profile. **j** The trajectories of Zn micromotors were recorded at the junction of channel A and B (*n* = 15 independent samples). k) Statistics on the moving direction distribution of Zn micromotors at the junction of channel A and B (*n* = 15 independent samples). **l** The trajectory of Zn micromotors was recorded at the junction of channel B and C (*n* = 15 independent samples). **m** Statistics on the moving direction distribution of Zn micromotors at the junction of channel B and C (*n* = 15 independent samples). Data in **b**–**g** and **j**–**m** represented as mean values ± S.D. *P* values were analyzed by Student's *t*-test (two-tailed). The asterisks (*) denote statistical significance: $^{**}p < 0.01$, $^{*}p < 0.05$. Source data are provided as a Source Data file. Some elements in this figure are reproduced from the MATRIX resource library, copyright Hangzhou SPHERE Tech. Ltd.

were replaced with DI water, i.e., after placing the water-soaked cotton (10 μL) in chambers A and B, respectively, the movement of Zn micromotors was observed near point C. According to the motion trajectory diagram and angle diagram of Zn micromotors (Supplementary Fig. 15a, b), it did not show the collective movement towards chamber B. It indicated that the chemotactic movement of Zn micromotors was not drift. Secondly, in order to investigate the influence of convection on the movement of Zn micromotors, $NH_3{\cdot}H_2O$ was replaced by inert NaCl solution (150 mM) and the cotton was soaked with 10 μL NaCl solution and placed in chamber B, while other parameters were kept the same with the experiment group. The movement of the Zn micromotors was observed near the point C. According to the trajectory and angle diagrams of the Zn micromotors (Supplementary Figs. 16a, b), the Zn micromotors were caused to move in the diffusion direction of the NaCl solution (to the left, not towards the NaCl solution) for a small distance. Thirdly, the $NH_3{\cdot}H_2O$ in chamber B was replaced with 150 mM NH_4Cl solution. As shown in Supplementary Fig. 17a, b, when Zn micromotors encounter NH_4Cl solution, they are similarly affected, and caused to move for a short distance along with the diffusion direction of NH_4Cl solution (to the left) and then stop. It was proved that the chemotactic process of Zn micromotors was mediated by $NH_3{\cdot}H_2O$ molecules. The above results shown that $NH_3{\cdot}H_2O$ could activate the chemotactic moving of Zn micromotors.

To explore the chemotactic principle of Zn micromotors, the products of Zn micromotors reacting with $NH_3{\cdot}H_2O$ were first detected by electrospray ionization mass spectrometry (ESI-MS) (Fig. 4e, and Supplementary Figs. 18, 19). After mass spectrometry analysis, the production of target complex ions $[Zn(NH_3)_1](OH)^+$, $[Zn(NH_3)_2](OH)^+$ were preliminarily determined. Thus the chemotactic behavior of the Zn micromotors was mainly due to their chemical reaction with $NH_3{\cdot}H_2O$:

$$2Zn + 4H_2O + 3NH_3 \rightarrow [Zn(NH_3)_1](OH)_2 + [Zn(NH_3)_2](OH)_2 + 2H_2$$

Excessive $NH_3{\cdot}H_2O$ reacted with Zn in a coordination reaction to form the complex ion. Due to the diffusion of $NH_3{\cdot}H_2O$, a concentration gradient was formed, with higher concentrations closer to chamber B. To validate the mechanism of chemotactic movement of the Zn micromotors towards ammonia, the chemotactic behavior of the Zn micromotors was simulated using finite element analysis software (COMSOL Multiphysics). First, the $NH_3{\cdot}H_2O$ source is set on the right side and gradually spreads to the left. Because the ion product complex ions $[Zn(NH_3)_1](OH)^+$ and $[Zn(NH_3)_2](OH)^+$ from the reaction have a slower diffusion rate than OH^-, more cations cluster around Zn micromotors. Due to the asymmetry of Zn micromotors, the cation concentration on the right side near the $NH_3{\cdot}H_2O$ source is higher than that on the left side (Fig. 4f). In order to maintain electrical neutrality, a local electric field is generated. The potential on the right side of Zn micromotors is higher than that on the left side. Since Zn micromotors are negatively charged, their movement direction is towards the high potential (right side). As shown in Fig. 4g, the simulated flow field around the Zn micromotor is from right to left (red arrow), so the movement direction of the Zn micromotor is to the right, and the maximum velocity of the flow field around the Zn micromotors is 5.82 × 10^{-5} m/s.

Cytological evaluation of the therapeutic effect of Zn micromotors in vitro

AML-12, a mouse normal hepatocyte, and HT22, a mouse hippocampal neuronal cell, were selected for cell oxidative stress, proliferation, and cell migration experiments. When cells are under oxidative stress, mitochondria and biomolecules can be damaged, leading to cell death or tissue damage. Under normal physiological conditions, the body can maintain the oxidative antioxidant dynamic balance through enzymes (superoxide dismutase (SOD), glutathione peroxidase (GSH PX) etc). Membrane lipid peroxidation often occurs after cell aging or damage, and malondialdehyde MDA is the final decomposition product of membrane lipid peroxidation, and its content reflects the degree of cell damage. Therefore, we selected three oxidative stress indicators, GSH, SOD and MDA, to detect the damage degree of ammonia to hepatocytes and neuron cells, and further investigated whether Zn micromotor could reduce the degree of cellular oxidative stress.

Different concentrations of ammonia (0 μM, 20 μM, 80 μM, 200 μM, 500 μM, 1000 μM) were added to the AML-12 medium of mouse normal hepatocytes and HT22 medium of hippocampal neuronal cells. After adding Zn micromotors, the cells were incubated for 48 h to detect the degree of oxidative stress. The results of oxidative stress detection of AML-12 in mouse normal hepatocytes showed that the GSH levels of AML-12 hepatocytes co-cultured with Zn micromotors were significantly increased at 20 μM (increased 31.10%), 80 μM (increased 53.07%) and 200 μM (increased 43.65%) ammonia concentration (Fig. 5a). The levels of SOD in AML-12 cells added with Zn micromotors in 20 μM (increased 70.59%), 80 μM (increased 59.62%), 500 μM (increased 43.06%) and 1000 μM (increased 60.44%) ammonia concentration groups were significantly increased (Fig. 5b). After adding Zn micromotors, the MDA level of AML-12 cells in 20 μM (decreased 36.45%), 80 μM (decreased 40.18%), 200 μM (decreased 40.94%), 500 μM (decreased 49.16%), and 1000 μM (decreased 50.12%) ammonia concentration groups significantly decreased (Fig. 5c).

The results of oxidative stress detection of HT22 cells in mouse hippocampal neurons showed that the GSH level of HT22 cells co-cultured with Zn micromotors did not significantly improve under different ammonia concentrations (Fig. 5d). The SOD levels of HT22 cells added with Zn micromotors in 20 μM (increased 32.34%), 80 μM (increased 23.39%), 500 μM (increased 39.21%) and 1000 μM (increased 46.09%) ammonia concentration groups were significantly

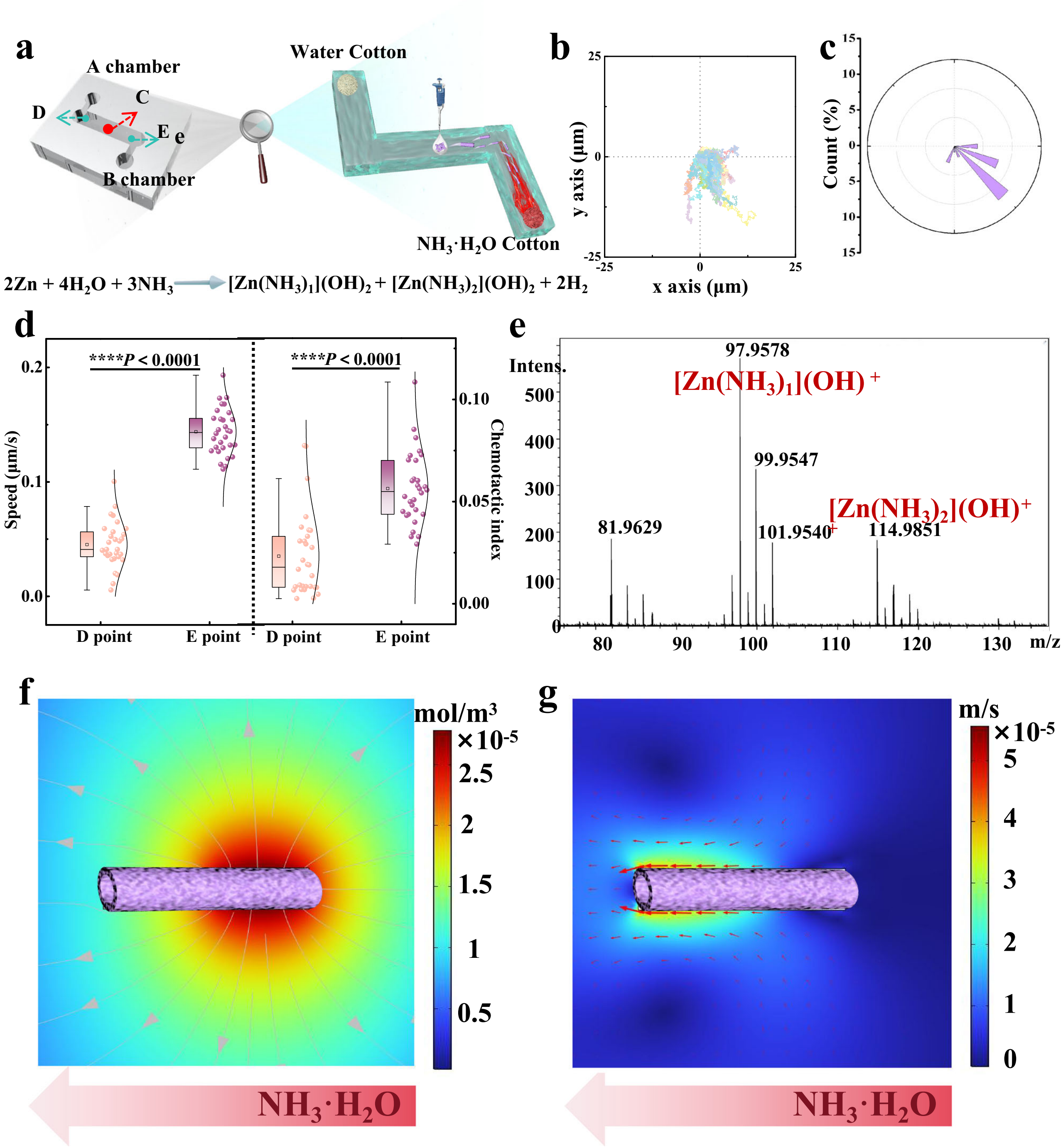

Fig. 4 | Evaluation of chemotaxis dynamics of Zn micromotors in channel. **a** Schematic diagram of chemotactic motion of Zn micromotors in channel. **b** Normalized motion trajectories and **c** Record the corresponding statistical data of the distribution of the movement direction of the Zn micromotor (*n* = 30 independent samples) at point E (near the cotton soaked in 150 mM ammonia solution). **d** Comparison of the movement speed and CI values of each group (*n* = 30 independent samples). Results were shown as box plots (The box represents the interquartile range (IQR), with the middle line indicating the median, the top and bottom edges of the box show the upper (Q3) and lower (Q1) quartiles respectively, while the whiskers extend to the maximum and minimum values of the dataset.) DI Water is control group. **e** ESI-MS of reaction products between Zn micromotors and $NH_3{\cdot}H_2O$. The experiment was repeated independently three times with similar results, and a representative result is shown. **f** Concentration field of Zn micromotor simulated by COMSOL, a multi-physics field finite element analysis software. **g** Velocity field of Zn micromotor simulated by COMSOL, a multi-physics field finite element analysis software. Data in **b**–**d** represented as mean ± S.D. *P* values were analyzed by Student's *t*-test (two-tailed). The asterisks (*) denote statistical significance: $^{****}p < 0.0001$. Source data are provided as a Source Data file. Some elements in this figure are reproduced from the MATRIX resource library, copyright Hangzhou SPHERE Tech. Ltd.

increased (Fig. 5e). After adding Zn micromotors, the MDA levels of HT22 cells in 20 μM (decreased 38.23%), 80 μM (decreased 50.34%), 200 μM (decreased 55.75%), 500 μM (decreased 49.90%), and 1000 μM (decreased 51.26%) ammonia concentration groups were significantly reduced (Fig. 5f). The above experimental results shown that ammonia would cause oxidative stress to cells, and the treatment of Zn micromotors can improve the degree of oxidative stress of AML-12 cells and HT22 cells.

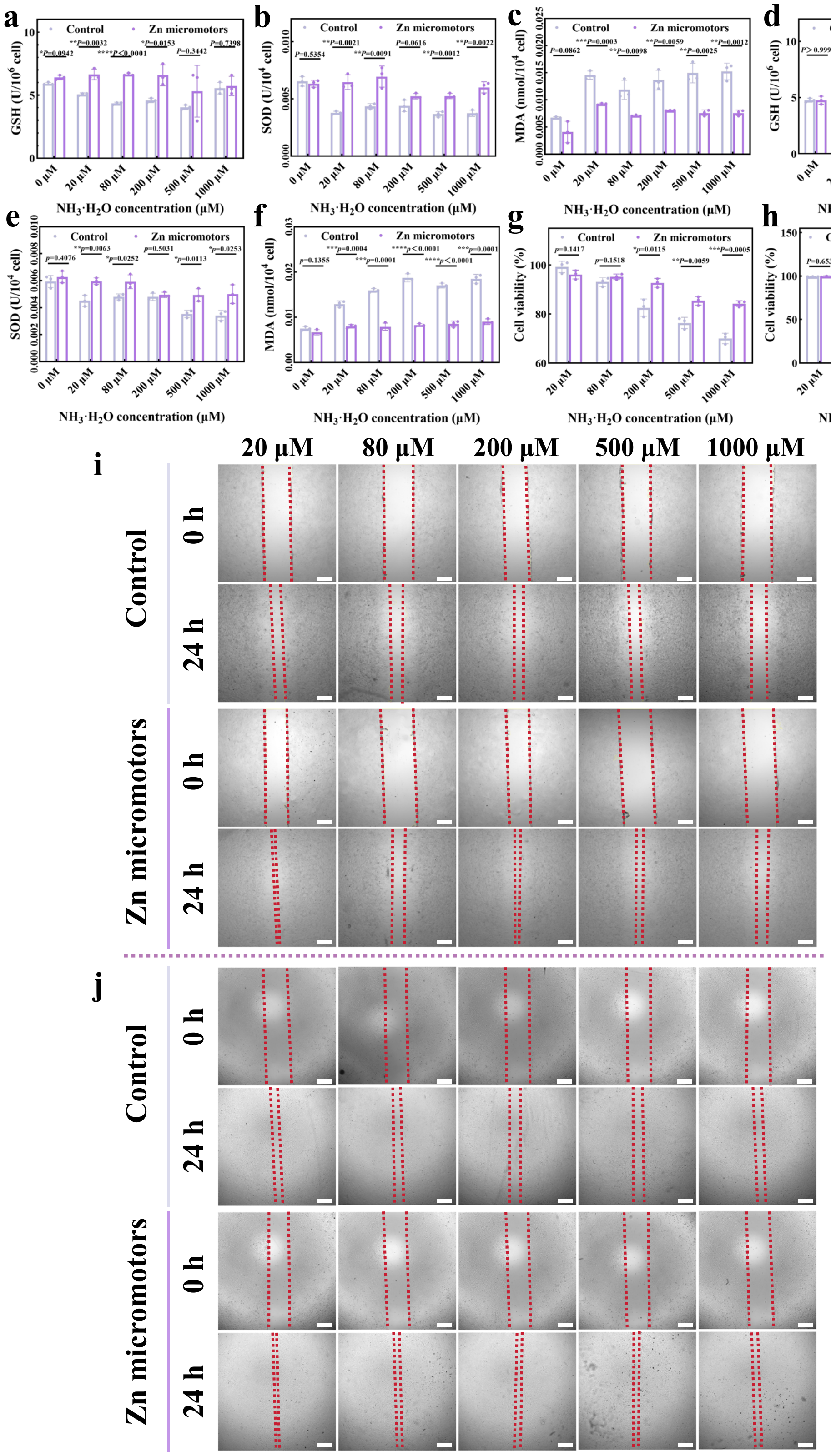

Fig. 5 | Therapeutic effect of Zn micromotors on ammonia treated cells. Oxidative stress indicators **a** GSH, **b** SOD and **c** MDA of AML-12 cells ($n = 3$ independent samples). Oxidative stress indicators **d** GSH, **e** SOD and f) MDA of HT22 cells ($n = 3$ independent samples). **g** Cell viability of AML-12 cells and **h** HT22 cells ($n = 3$ independent samples). **i** Cell migration image of AML-12 cells and **j** HT22 cells. The experiment was repeated independently three times with similar results, and a representative result is shown. Scale bar: 500 µm. Data in a-h represented as mean ± S.D. *P* values were analyzed by Student's *t*-test (two-tailed). The asterisks (*) denote statistical significance: ****$p < 0.0001$, ***$p < 0.001$, **$p < 0.01$, *$p < 0.05$. Source data are provided as a Source Data file.

At the same time, we detected the effect of different concentrations of ammonia environment on cell proliferation, and the improvement of the environment by the addition of Zn micromotors. As shown in Fig. 5g, a low concentration of ammonia (20 μM, 80 μM) environment had no significant effect on the activity of AML-12 cells. With the increase of ammonia concentration, the activity of AML-12 cells decreased, but it was improved after the co-culture of Zn micromotors. The activities of the 200 μM, 500 μM, and 1000 μM groups were significantly increased by 12.27%, 11.82%, and 20.25%, respectively. The above results show that an ammonia environment will reduce cell viability, and Zn micromotors can improve the environment and promote cell proliferation. As shown in Fig. 5h, there was no significant effect on the activity of HT22 cells except for ammonia concentrations of 1000 μM and 200 μM.

Next, we used the cell scratch assay to evaluate the cell migration ability. The experiment was set up with a control group (adding different concentrations of ammonia into the cell culture medium) and a Zn micromotor group (adding ammonia and Zn micromotors into the cell culture medium at the same time). The results were obtained by comparing the scratch area of AML-12 in two groups of normal hepatocytes at 0 h and 24 h. Results as shown in Fig. 5i and Supplementary Fig. 20, after 24 h, the healing area of Zn micromotor group increased by 38.35% compared with the control group (20 μM $NH_3·H_2O$); Compared with the control group (200 μM $NH_3·H_2O$), the healing area increased by 26.35%. Furthermore, in comparison to the control group with 500 μM $NH_3·H_2O$, the healing area increased by 29.37%, and with 1000 μM $NH_3·H_2O$, the healing area increased by 16.90%. The results obtained by comparing the scratch area of two groups of hippocampal neuronal cells, HT22 at 0 h and 24 h were shown in Fig. 5j and Supplementary Fig. 21. After 24 h, the healing area of Zn micromotor group increased by 37.75% compared with control group (20 μM $NH_3·H_2O$). The other groups were also significantly improved. In comparison to the control group with 80 μM $NH_3·H_2O$, the healing area increased by 29.98%; with 200 μM $NH_3·H_2O$, the healing area increased by 24.22%; with 500 μM $NH_3·H_2O$, the healing area increased by 22.09%; and with 1000 μM $NH_3·H_2O$, the healing area increased by 28.87%. The above results of cell migration show that ammonia can affect the cell migration rate, and Zn micromotors can promote the recovery of cell mobility and improve the cell migration rate.

According to the above cell experiments, excessive ammonia in the cell culture environment will lead to oxidative stress and reduced proliferation of hepatocytes/neuron cells. The addition of Zn micromotors can improve the cell culture environment, thus reducing the oxidative stress injury of cells, promoting the proliferation and migration of cells.

Pharmacodynamic evaluation of Zn micromotors in vivo

Intraperitoneal injection of thioacetamide (TAA) induced persistent hepatocellular injury and fibrosis (Fig. 6a). A model dose of 100 mg/kg was used, and the model duration was 6 weeks. Due to pathological conditions such as liver cell damage, ammonia cannot be metabolized smoothly, leading to hyperammonemia. Here, Zn micromotors were used for treatment. Due to the fact that the organs responsible for ammonia production and metabolism are the colon and liver, where ammonia accumulates in large quantities, treatment methods are divided into oral and intravenous injections.

We initially investigated the dosage of Zn micromotors by designing pharmacodynamic pre-tests in low (0.5 mg/kg), medium (2 mg/kg), and high (3.5 mg/kg) Zn micromotor dose groups. After 6 weeks of modeling and treatment, the degree of liver injury was assessed by measuring the levels of aspartate aminotransferase (AST), alanine aminotransferase (ALT), albumin (ALB), total bilirubin (TBIL) released by the liver into the blood, and the blood ammonia concentration. As shown in Supplementary Fig. 22a, compared with the control group, the blood ammonia concentration in the TAA group significantly increased by 3.72 times. Zn micromotor (i.v.) group showed a significant decrease in blood ammonia concentration by 15.94%, 54.49%, and 20.93% in all the groups (0.5 mg/kg group, 2 mg/kg group, 3.5 mg/kg group) as compared to the TAA group. Zn micromotor (i.g.) group showed a significant decrease in blood ammonia concentration by 3.31%, 44.25%, and 50.70% in all the groups (0.5 mg/kg group, 2 mg/kg group) as compared to the TAA group.

To assess the extent of liver damage caused by high blood ammonia, biochemical tests of liver function were conducted. As shown in Supplementary Fig. 22b-e, compared with the control group, AST, ALT, and TBIL activities were significantly higher in the TAA group, increasing by 7.10, 10.41, and 0.72 times, ALB activity was significantly lower in the TAA group, reducing by 0.22 times. The Zn micromotor (i.v.) group and Zn micromotor (i.g.) group demonstrated some improvement after treatment. In the Zn micromotor (i.v.) group (0.5 mg/kg, 2 mg/kg, 3.5 mg/kg), the AST value of 2 mg/kg dose group significantly decreased by 60.92%, and the AST value of 0.5 mg/kg and 3.5 mg/kg decreased by 37.86% and 52.12%, respectively. The Zn micromotor (i.v..) group (2 mg/kg, 3.5 mg/kg) with significant decreases in ALT values by 75.22% and 75.41%, and in ALT values at the low dose (0.5 mg/kg), it decreased by 37.31%. The Zn micromotor (i.v.) group (2 mg/kg, 3.5 mg/kg) with significant decreases in TBIL values by 30.09% and 31.28%, compared with the TAA group. There was no significant difference in TBIL and ALB values between the low-dose (0.5 mg/kg) group and the TAA group. ALB activity in the medium and high dose groups (2 mg/kg, 3.5 mg/kg) was significantly increased by 21.74% and 18.69%, respectively. AST in the 0.5 mg/kg dose group of the Zn micromotor (i.g.) group, 0.5 mg/kg, 2 mg/kg, 3.5 mg/kg), there was no significant difference in ALT and TBIL activities between the two groups. There was no significant difference in ALB values between the Zn micromotor (i.g.) group and the TAA group at all doses. The AST values in the Zn micromotor (i.g.) group (2 mg/kg, 3.5 mg/kg) significantly decreased by 34.77% and 48.05%, respectively, while the ALT values significantly decreased by 47.40% and 63.07%, respectively, TBIL values significantly decreased by 25.64% in the Zn micromotor (i.g.) group (3.5 mg/kg), respectively.

According to the above biochemical detection results, the liver damage of TAA group mice was more serious. After treatment with Zn micromotors, the liver damage of Zn micromotor (i.v.) group and Zn micromotor (i.g.) group mice was alleviated. After an overall analysis of the blood biochemistry test results, it was found that the medium-dose group (2 mg/kg) and high-dose group (3.5 mg/kg) of the Zn micromotor (i.v.) had better treatment effects, and the treatment effects were similar. The therapeutic effect of the high dose group (3.5 mg/kg) of Zn micromotor (i.g.) was superior to the other two groups.

Next, we examined the degree of oxidative stress in liver tissue. Oxidative stress biomarkers include: Glutathione (GSH), the main free radical scavenger in the body, has antioxidative and detoxifying effects. Superoxide dismutase (SOD) is an important metal enzyme in the human antioxidant process, which can catalyze the decomposition of superoxide anion radicals into oxygen and hydrogen peroxide. MDA is a product of lipid peroxidation by free radicals, which can indirectly reflect tissue peroxidation damage. As shown in Supplementary Fig. 22f–h, compared with the control group, the GSH content in the liver of the TAA group decreased by 44.00%, the T-SOD value was significantly reduced by 53.07%, and the TAA group showed a significant increase in MDA of 62.33%. Comparison between Zn micromotor (i.v.) group and TAA group, GSH content in (2 mg/kg) group increased by 1.08 times, there was no significant difference between the low-dose (0.5 mg/kg) and high-dose (3.5 mg/kg) groups. The T-SOD value of 2 mg/kg and 3.5 mg/kg groups was significantly increased by 89.37% and 61.46%, while there was no significant difference between the 0.5 mg/kg group compared with the TAA group. The MDA value of the 2 mg/kg and 3.5 mg/kg groups was significantly reduced by 44.78% and 53.12%, while there was no significant

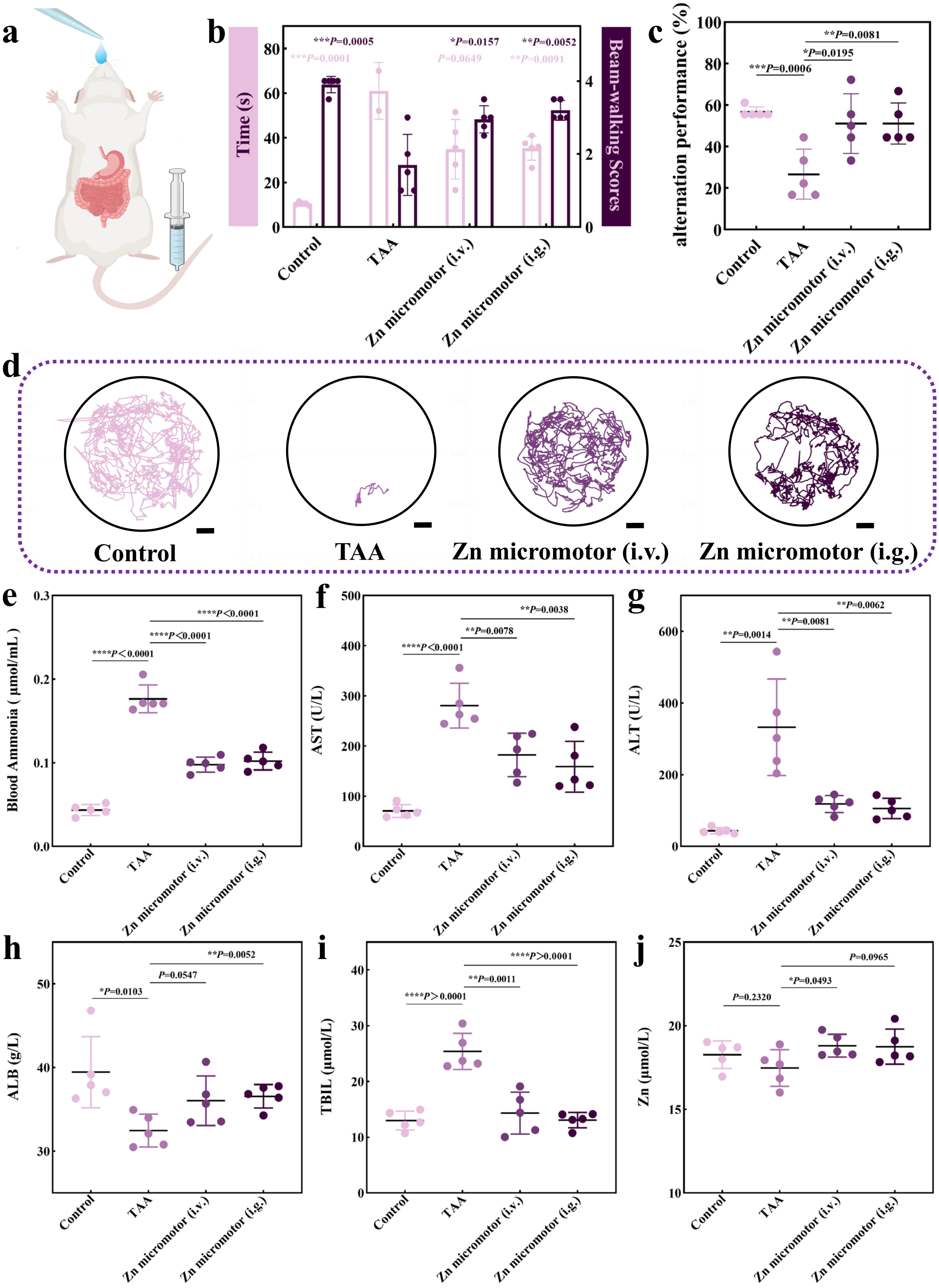

Fig. 6 | Evaluation of moving activity and biochemical tests of liver function in mice after Zn micromotor treatment. **a** Schematic diagram of mouse treatment. **b** The balance beam test (*n* = 5 independent samples). **c** Y-maze spontaneous alternation experiment (*n* = 5 independent samples). **d** Motion trajectories after molding and treatment. Scale bar: 2 cm. **e** Ammonia. **f** AST. **g** ALT. **h** ALB. **i** TBIL. and **j** Zn levels in serum (*n* = 5 independent samples). Data in **b**–**j** represent as mean ± S.D. *P* values were analyzed by Student's *t*-test (two-tailed). The asterisks (*) denote statistical significance: ****$p < 0.0001$, **$p < 0.01$, *$p < 0.05$. Source data are provided as a Source Data file. Some elements in this figure are reproduced from the MATRIX resource library, copyright Hangzhou SPHERE Tech. Ltd.

difference between the 0.5 mg/kg group compared with the TAA group. Comparison between Zn micromotor (i.g.) group and TAA group, GSH content in the (2 mg/kg) group increased by 0.50 times, there was no significant difference between the low-dose (0.5 mg/kg) and high-dose (3.5 mg/kg) groups. The T-SOD value of the 2 mg/kg and 3.5 mg/kg groups was significantly increased by 57.77% and 80.50%, while there was no significant difference between the 0.5 mg/kg group compared with the TAA group. The MDA value of 0.5 mg/kg and 3.5 mg/kg groups was significantly reduced by 48.59% and 51.26%, while there was no significant difference between 2 mg/kg group compared with the TAA group.

We use histological sectioning, also known as Sirius Red staining, to examine the degree of liver injury and fibrosis. The staining area of Sirius Red on collagen fibers was quantified using ImageJ software, and the area proportion of collagen fibers was calculated. As shown in Supplementary Fig. 22i and j, the liver tissue of mice in the control group showed no obvious fibroproliferation, and the tissue structure remained intact. In contrast, the area percentage of collagen fibers in the TAA group was increased by 36.56 times compared to the control group. The area percentage of collagen fibers in the Zn micromotor (i.v.) group (2 mg/kg, 3.5 mg/kg) was decreased by 79.23% and 67.71%, respectively, compared to the TAA group. The area percentage of collagen fibers in the Zn micromotor (i.g.) group (2 mg/kg, 3.5 mg/kg) was decreased by 65.03% and 74.64%, respectively, compared to the TAA group. This further confirmed that Zn micromotors were dose-dependent in the treatment of hyperammonemia. After the results of the experiment were statistically analyzed, the group with the best therapeutic effect dose was selected for the following in vivo experimental study. The optimal dose for Zn micromotor (i.v.) group is 2 mg/kg. The optimal dose for the Zn micromotor (i.g.) group is 3.5 mg/kg.

Zn micromotors on behavior of TAA-induced hyperammonemia mice

Due to liver damage, liver function was impaired, reducing the liver's metabolic function and leading to nutritional imbalances and conditions such as loss of appetite, which resulted in weight loss. After one week of modeling, the weight of the control group increased by 0.33% ± 0.79, and the weight of the TAA, Zn micromotor (i.v.), and Zn micromotor (i.g.) groups decreased significantly by 3.10% ± 4.03, 2.72% ± 1.01, 1.33% ± 5.09, respectively. After 3 weeks of Zn micromotor treatment, the body weight of the TAA group significantly decreased by 6.51% ± 2.82, and those of Zn micromotor (i.v.) and Zn micromotor (i.g.) groups decreased by 0.09% ± 2.82 and 1.60% ± 4.58, respectively. After 7 weeks of Zn micromotor treatment, compared to the previous treatment, the control group and Zn micromotor (i.v.) group gained weight by 4.01% ± 7.46 and 4.53% ± 6.22, respectively. The TAA and Zn micromotor (i.g.) groups lost 7.82% ± 4.26 and 5.52% ± 3.23 of body weight, respectively (Supplementary Fig. 23).

The liver was stimulated by TAA for a long time, and excessive collagen deposition led to diffuse fibrosis of liver tissue, which destroyed the structure of liver cells, prevented normal metabolism of blood ammonia, and caused an increase in blood ammonia. Abnormally high levels of ammonia in the blood can disrupt neurotransmitter metabolism, adversely affecting the function of the peripheral nervous system. This disruption can decrease the excitability of the neuromuscular junction, causing muscle contractions to lose their coordination. As a result, moving abnormalities such as limb weakness, spasticity, and paralysis may occur. Consequently, we have preliminarily evaluated the moving behavior of mice to understand these effects better.

First, the mouse balance beam test was set up to evaluate the coordination and balance ability of mice by evaluating the ability of mice to walk on the balance beam. In this study, we tested the balance ability of different groups of mice on a 6-mm beam, recorded the time taken by the mice to pass the 80 cm distance and scored the neural behavior. In Fig. 6b, the results showed that compared with the control group (Healthy mice), the time that mice spent on traversing the beam in the TAA group was prolonged by 486.54% (control 10.4 ± 0.74 s, TAA 61 ± 12.73 s). Zn micromotor (i.v.) group and Zn micromotor (i.g.) group time was reduced by 42.95% and 42.13%, respectively, compared to the TAA group (Zn micromotor (i.v.) (34.8 ± 13.41) s, Zn micromotor (i.g.) (35.3 ± 5.37) s. These results indicated that TAA modeling resulted in impaired moving ability, decline of exercise ability and the prolongation of hurdle traversing time. After treatment with Zn micromotor, the damage of brain neurons caused by ammonia penetration was alleviated, and the exercise ability had a recovery. Then, we scored the mice through their behavioral performance (smooth crossing; keeping balance, slipping, and footstep sound) in the process of crossing the beam to evaluate their motor function and balance ability. Behavioral scores decreased by 56.41% in the TAA group compared to the control group. After Zn micromotor treatment, Zn micromotor (i.v.) group and Zn micromotor (i.g.) group scores improved by 73.53% and 88.24%, respectively. The results showed that the Zn micromotor intervention led to an improvement in neurobehavioral scores.

Next, the Y-maze spontaneous alternation experiment was incorporated to test the cognition and spatial working memory of mice. As shown in Fig. 6c, the spontaneous alternation behavior ability of TAA model mice was significantly decreased by 52.94% compared with that of the control group mice. Following treatment, the spontaneous alternation behavior ability of the Zn micromotor (i.v.) group and Zn micromotor (i.g.) group showed a notable improvement of 91.67% when compared with the TAA group. The results suggested that excessive ammonia permeation of the brain causes spatial working memory bias in mice, and that treatment with Zn micromotors can effectively alleviate brain damage and improve cognitive function in mice.

Finally, to assess the exercise capability of mice, a round glass container was prepared to allow free movement (Supplementary Fig. 24). Mice were tracked and filmed for their motion during the week following treatment (Supplementary Movies 9–12). The tracking results are illustrated in Fig. 6d. The total active distance of mice in the control group was 698.19 ± 4.44 cm, and the average speed was 2.33 ± 0.01 cm/s. Compared with the control group, the total distance for the TAA group decreased to 57.32 ± 0.35 cm, with an average speed of 0.19 ± 0.001 cm/s. Relative to the TAA group, both the total path and speed of movement in the Zn micromotor treatment groups showed significant improvements. The total distance (583.44 ± 1.54) cm and average speed (1.94 ± 0.01) cm/s of the Zn micromotor (i.v.) group increased by 9.18 times and 9.21 times, respectively. The total distance (533.97 ± 1.70) cm and average speed (1.78 ± 0.01) cm/s of Zn micromotor (i.g.) group were increased by 8.32 times and 8.37 times, respectively. From the perspective of behavior, the treatment of Zn micromotors can improve the motor dysfunction of hyperammonemic mice.

Effects of Zn micromotors on blood ammonia concentration and liver function in TAA-induced hyperammonemia mice

The above experimental results indicated that the mice had developed abnormalities in their behavior and the model was initially judged to be valid from a behavioral point of view. Next, the distribution of Zn micromotors in organs in vivo was observed through in vivo imaging experiments. In the in vivo imaging experiment, in addition to the Zn micromotor treatment group, we also set up an inert control group. The inert control group was inert gold control particles (3 μm in length) of the same length of Zn micromotors. Because the fluorescent probe Zinpyr-1 can only specifically label Zn, we chose FITC fluorescence with a fluorescence wavelength close to that of Zinpyr-1 to fluorescently label gold particles. As shown in Supplementary Fig. 25a, the position marked by the white circle is the position of the liver. Compared with the gold particle control group, the liver targeting of

TAA model mice in the Zn micromotor group was significantly enhanced. According to the organ distribution map (Supplementary Fig. 25b), the distribution of gold particles in the liver accounted for 12.16% of all organs, and the distribution of Zn micromotors in the liver accounted for 20.01% of all organs. Based on the above experimental results, it can be concluded that Zn micromotors have a stronger targeting of the liver. It facilitates capturing excess ammonia in the liver.

Subsequently, the degree of liver injury was assessed by measuring the levels of aspartate aminotransferase (AST), alanine aminotransferase (ALT), albumin (ALB), total bilirubin (TBIL) released by the liver into the blood, and the blood ammonia concentration. Additionally, the Zn content in the body was monitored to ensure that its levels were not excessive. As shown in Fig. 6e, compared with the control group, the blood ammonia concentration in the TAA group significantly increased by 3.05 times, and the Zn micromotor (i.v.) group and Zn micromotor (i.g.) group significantly decreased by 44.59% and 42.13%, respectively, compared with the TAA group. If the liver fails to convert ammonia into urea to be excreted from the body, the level of ammonia in the blood will rise, which can be used to identify abnormal liver function.

To assess the extent of liver damage caused by high blood ammonia, biochemical tests of liver function were conducted. Compared with the control group, AST and ALT activities were significantly higher in the TAA group, increasing by 2.98 and 6.62 times, respectively. The Zn micromotor (i.v.) group and Zn micromotor (i.g.) group demonstrated some improvement after treatment, with significant decreases in AST values by 35.00% and 43.35%, and in ALT values by 64.40% and 68.27%, respectively, compared to the TAA group (Fig. 6f, g). ALB, which is only synthesized in the liver, decreases when the liver is damaged. ALB values in TAA group, Zn micromotor (i.v.) group and Zn micromotor (i.g.) group all decreased to some extent, though ALB values in the Zn micromotor (i.g.) group slightly recovered, increasing by 12.64% compared with the TAA group (Fig. 6h). The TBIL value in TAA group was 0.96 times higher than that in the control group, and the Zn micromotor (i.v.) group and Zn micromotor (i.g.) group were 43.66% and 48.56% lower than that in TAA group, respectively (Fig. 6i). Bile acids, which are synthesized and secreted in the liver, also show abnormal elevations when liver cells are damaged and bile is not excreted properly. Finally, the concentration of Zn in the serum was detected. The Zn concentration in the Zn micromotor (i.v.) group was 0.08 times higher than that in the TAA group, with no significant differences between the other groups (Fig. 6j). According to the above biochemical detection results, the liver damage of TAA group mice was more serious, and the liver damage of Zn micromotor (i.v.) group and Zn micromotor (i.g.) group mice was alleviated.

Zn micromotors alleviate oxidative stress in TAA-induced hyperammoniated mouse liver

Based on the determination of abnormal liver function, we then calculated the ratio of liver to body weight. An abnormal increase in this ratio suggests that the liver may be in a pathological state, such as edema, hyperplasia, fibrosis, or fatty liver. Compared with the control group, the liver weight of the other three groups of mice increased abnormally, with the ratio of liver to body weight in the TAA group increasing by 63.03%. The Zn micromotor (i.v.) group and the Zn micromotor (i.g.) group showed a decrease in the ratio of liver to body weight by 21.50% and 21.94%, respectively, compared to the TAA group (Fig. 7a). This indicated an improvement in the abnormal enlargement of the liver.

We detected the decline rate of ammonia in blood and liver, respectively. First, the blood ammonia levels and their rate of decrease were examined separately in mice from the Zn micromotor (i.v.), Zn micromotor (i.g.), and TAA groups. As shown in Fig. 7b, after intravenous and intragastric administration of Zn micromotor, the initial blood ammonia concentrations were 0.110 μmol/ml for the Zn micromotor (i.v.) group, 0.206 μmol/ml for the Zn micromotor (i.g.) group, and 0.221 μmol/ml for the TAA group. The blood ammonia of Zn micromotor (i.v.) group decreased by 10.29% after 0.5 h and 30.08% after 3 h. Subsequently, a gradual reduction was observed, leading to a decrease of 51.72% after 12 h, reaching a concentration of 0.053 μmol/ml, approximating the normal value. The Zn micromotor (i.g.) group exhibited substantial reductions in blood ammonia levels, with decreases of 37.87% at 0.5 h, 53.44% at 3 h, and a remarkable drop of 70.69% to 0.060 μmol/ml after 12 h. Conversely, the TAA group experienced a minor increase in blood ammonia at 0.5 h, followed by a decline of 34.86% after 3 h and a decrease of 0.116 μmol/ml after 12 h, representing a reduction of 47.44%. Even after 24 h, the blood ammonia levels in the TAA group did not return to the normal range.

Next, the ammonia levels and their decline rates in the liver of mice in the Zn micromotor (i.v.) group, Zn micromotor (i.g.) group, and TAA group were determined. As shown in Fig. 7c, after intravenous and intragastric administration of Zn micromotors, the initial blood ammonia concentration of the Zn micromotor (i.v.) group was 1.79 μg/g, Zn micromotor (i.g.) group was 3.65 μg/g, and the TAA group was 4.23 μg/g. Notably, the Zn micromotor (i.v.) group showed a decrease of 8.35% in liver ammonia within 0.5 h, 33.57% after 3 h, and 68.64% after 24 h, with a liver ammonia concentration of 0.56 μg/g. The blood ammonia of Zn micromotor (i.g.) group decreased by 12.95% after 0.5 h, 41.00% after 3 h. Blood ammonia decreased to 0.67 μg/g after 24 h, with an overall decrease of 81.92%. In the TAA group, a minimal increase in blood ammonia was observed at 0.5 h, followed by a reduction of 29.93% at 3 h, and ultimately a concentration of 1.37 μg/g at 24 h, corresponding to an overall decrease of 67.68%.

In conclusion, ammonia in both blood and liver decreases with time, and content of ammonia in the Zn micromotor treatment group can drop to near normal value within 12 h, while the content of ammonia in the TAA group within 24 h is difficult to drop to normal value.

Oxidative stress, characterized by the excessive accumulation of reactive oxygen species (ROS) in the body, leads to inflammatory infiltration of neutrophils and promotes an inflammatory response in local tissues. Liver tissue was analyzed for oxidative stress markers. Glutathione (GSH), a key scavenger of ROS and the main free radical scavenger in the body, has antioxidative and detoxifying effects. Compared with the control group, the GSH content in the liver of the TAA group decreased by 16.05%. Compared with TAA group, GSH content in Zn micromotor (i.v.) group and Zn micromotor (i.g.) group increased by 0.30 times and 0.34 times, and the level was similar to that of normal mice (Fig. 7d). Superoxide dismutase (SOD), a crucial metalloenzyme in the body's antioxidant process, catalyzes the dismutation of superoxide anion radicals into oxygen and hydrogen peroxide. The T-SOD value of TAA group was significantly reduced by 27.98%, while there was no significant difference between Zn micromotor (i.v.) group and Zn micromotor (i.g.) group compared with the control group (Fig. 7e). In human body, MDA is the product of lipid peroxidation by free radicals. It is cytotoxic and can indirectly reflect tissue peroxidation damage. The TAA group showed a significant increase in MDA of 28.5% compared with the control group, and the MDA value of Zn micromotor (i.v.) group was increased, but there was no significant difference with the control group (Fig. 7f). Thus, Zn micromotors can alleviate oxidative stress injury of liver tissue to a certain extent.

Histopathological observation of the liver in TAA-induced hyperammonemia mice

Firstly, intuitive histological sections were used to examine the liver damage and the degree of fibrosis. Firstly, liver tissue sections were stained with Sirius Red to evaluate the degree of fibroproliferation in liver lesions. The liver tissue of mice in the control group showed no obvious fibroproliferation, and the tissue structure remained intact

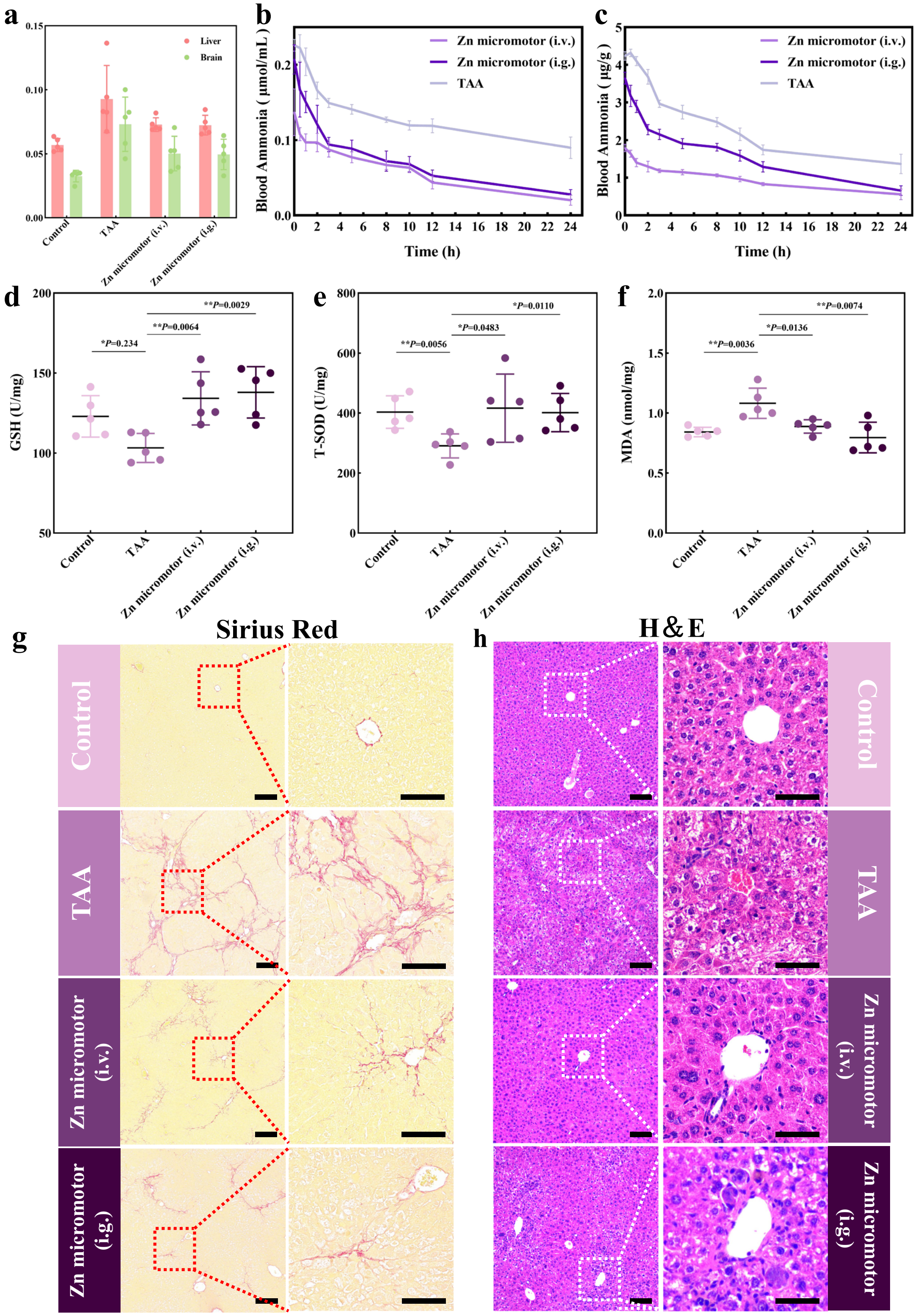

Fig. 7 | **Histopathological examination of the liver.** **a** Liver brain body weight ratio ($n = 5$ independent samples). **b** The decreasing rate of blood ammonia in mice of each group ($n = 3$ independent samples). **c** The decreasing rate of ammonia content in the liver of mice in each group ($n = 3$ independent samples). **d** GSH. **e** T-SOD. **f** MDA levels oxidative stress biomarkers in the liver ($n = 5$ independent samples). **g** Sirius-red staining images of liver tissue sections. Scale bar: 200 μm, 100 μm. **h** H&E stained images of liver tissue sections. Scale bar: 200 μm, 100 μm. Data in **d**–**f** represent as mean ± S.D. *P* values were analyzed by Student's *t*-test (two-tailed). The asterisks (*) denote statistical significance: $^{**}p < 0.01$, $^{*}p < 0.05$. Source data are provided as a Source Data file.

(Fig. 7g). In contrast, the liver of mice in the TAA group exhibited significant fibroproliferation with pseudolobule formation. Although fibroproliferation was also present in the liver tissue of the Zn micromotor treatment group, the degree of fibroproliferation was reduced, and liver tissue in the Zn micromotor (i.g.) group exhibited edema. The staining area of Sirius Red on collagen fibers was quantified using ImageJ software, and the area proportion of collagen fibers was calculated (Supplementary Fig. 26). The area percentage of collagen fibers in the TAA group was increased by 4.46 times compared to the control group. The area percentage of collagen fibers in the Zn micromotor (i.v.) group and Zn micromotor (i.g.) group was decreased by 38.33% and 31.81%, respectively, compared to the TAA group. This further confirmed that Zn micromotors can mitigate liver injury by reducing the blood ammonia level in vivo.

Secondly, the pathological characteristics of the liver were analyzed by H&E staining. In the control group, the liver tissue was structurally intact, the hepatocytes were arranged radially around the central vein, hepatocytes showed mild edema and degeneration, no definite steatosis was found, no obvious fibrous tissue hyperplasia was found in the portal area, and no definite inflammatory cell infiltration was found in the portal area (Fig. 7h). In the TAA group, the cytoplasm appeared as eosinophilic with loose red staining, and nuclei were round with occasional binucleation. Severe edema and degeneration of hepatocytes could be seen, ballooning change was observed, and no clear steatosis was seen. There was significant fibrous tissue hyperplasia and extensive inflammatory cell infiltration in the portal area, and bridging necrosis was noticeable between the portal areas and the central veins. The structure of the liver plate was unclear, liver sinusoids were narrowed, and slight inflammatory cell infiltration was observed within hepatocytes. In the Zn micromotor (i.g.) group, fibroplasia in the confluent area was reduced compared with the TAA group, and moderate edema and degeneration of hepatocytes were noted, with reduced ballooning areas. Compared with the TAA group, the Zn micromotor (i.v.) group still showed hepatocyte edema, but no obvious ballooning, and the proliferation of fibrous tissue in the portal area was significantly reduced. Liver fibrosis was evaluated by the liver pathology scoring system (Ishak semi-quantitative scoring system). The proliferation of fibrous tissue in the Zn micromotors treatment group was notably reduced compared to the TAA group, and the difference was statistically significant (Supplementary Fig. 27). The results demonstrated that Zn micromotors could alleviate liver injury caused by high blood ammonia.

Zn micromotors alleviate oxidative stress in the cerebral cortex of mice with TAA-induced hepatic encephalopathy

Upon the liver function was compromised, the circulating ammonia in the body could not be eliminated timely. Ammonia readily penetrated the blood-brain barrier in molecular form, and its excessive accumulation in the brain led to hepatic encephalopathy[44]. We detected the content changes of ammonia, glutamate, and glutamine in the brain. In Supplementary Fig. 28a, compared with the control group, the ammonia in brain tissue of the TAA group increased by 1.58 times. After treatment with Zn micromotors, the ammonia content in the brain tissue of Zn micromotor (i.v.) group and Zn micromotor (i.g.) group decreased by 40.22% and 24.46%, respectively. Glutamate is an excitatory neurotransmitter in the brain. Increased glutamate accumulation leads to brain injury, such as cerebral ischemia or hypoxia. Glutamine is an amino acid and a metabolite of ammonia. If the concentration of glutamine in the brain is too high, it will lead to brain edema or destroy the homeostatic environment. The metabolism of ammonia in the brain depends on the glutamine/glutamate cycle and the ability of brain to eliminate ammonia[45]. Therefore, we simultaneously detected the contents of glutamate and glutamine in brain tissues for each group. The content of glutamate in the TAA group was 31.24% higher than that in the control group. In a comparative analysis, the Zn micromotor (i.v.) group and the Zn micromotor (i.g.) group demonstrated reductions in glutamate content 11.98% and 15.82%, respectively, when contrasted with the TAA group (Supplementary Fig. 28b). Additionally, the glutamine content in the TAA group was found to be significantly elevated, with a 7.78-fold increase relative to the control group. After treatment, the glutamine content in the Zn micromotor (i.v.) group and the Zn micromotor (i.g.) group underwent a marked reduction, declining by 65.42% and 63.00%, respectively (Fig. 8a). The above experimental results showed that the content of ammonia, glutamate and ammonia metabolite glutamine in the brain with hepatic encephalopathy was high, and would further damage the brain. After treatment with Zn micromotors, ammonia and ammonia metabolites decreased.

Ammonia's significant neurotoxicity caused oxidative stress in the brain, resulting in neuronal damage. In the experiments conducted to evaluate hepatic encephalopathy due to hyperammonemia, a portion of cortical brain tissue was collected to detect oxidative stress biomarkers. The GSH level in the brain was reduced by 54.53% in the TAA group compared to the control group. Compared with the TAA group, GSH levels in the Zn micromotor (i.v.) group and the Zn micromotor (i.g.) group increased by 0.76 times and 0.70 times, and the levels were similar to that in the control group (Fig. 8b). T-SOD level was significantly decreased by 21.44% in TAA group, while the Zn micromotor (i.v.) group and Zn micromotor (i.g.) group increased by 0.52 times and 0.41 times compared with TAA group, respectively, with no significant difference compared with the control group (Fig. 8c). The MDA value had significantly increased by 33.05% in the TAA group. After treatment, the MDA values in the Zn micromotor (i.v.) and Zn micromotor (i.g.) groups decreased by 30.69% and 27.7%, respectively (Fig. 8d). The above experimental results showed that abnormal increase of blood ammonia in mice not only accelerated the formation of liver fibrosis, but also further caused a certain degree of damage to the brain. According to the detection results of oxidative stress markers, the treatment with Zn micromotors improved the oxidative stress injury of the cerebral cortex.

Histopathological observations on the brain of mice with TAA-induced hepatic encephalopathy

Hepatic encephalopathy causes cerebral edema and increased intracranial pressure, leading to central nervous system dysfunction characterized by cognitive, psychiatric, and motor deficits, accompanied by symptoms of reduced tone in the extremities. Preliminary evidence that hepatic encephalopathy significantly affected the neurological function of the brain was previously demonstrated in a behavioral study (Fig. 6b-d). The TAA group exhibited a significant decrease in moving ability. However, there was the recovery of the moving function following Zn micromotor treatment.

Then, H&E histopathology was conducted on the cortical and hippocampal regions of the brain (Supplementary Fig. 29). In the control group, the brain tissue structure appeared as normal, with neurons and astrocytes in the cerebral cortex and hippocampus being round and their nuclei intact; no obvious pathological edema or vacuolization was observed. The TAA group exhibited inflammatory cell infiltration, and neurons showed marked atrophy, degeneration, and apoptosis, particularly in the cortical areas of the brain. In the hippocampal CA1 and CA3 areas, there was evidence of nucleus regression and mild cell swelling. For the Zn micromotor (i.v.) and Zn micromotor (i.g.) groups, mild neuronal degeneration in the cortical area of the brain and mild cell swelling in the hippocampal CA3 area are observed. The H&E results indicated that treatment with Zn micromotors significantly improved the neuron injury in the cerebral cortex.

Next, to further investigate the fate of neurons after hepatic encephalopathy caused by hyperammonemia. Nissl staining and H&E staining were utilized to evaluate the damage to neurons. After Nissl staining, neurons that were abnormally atrophic and deeply stained

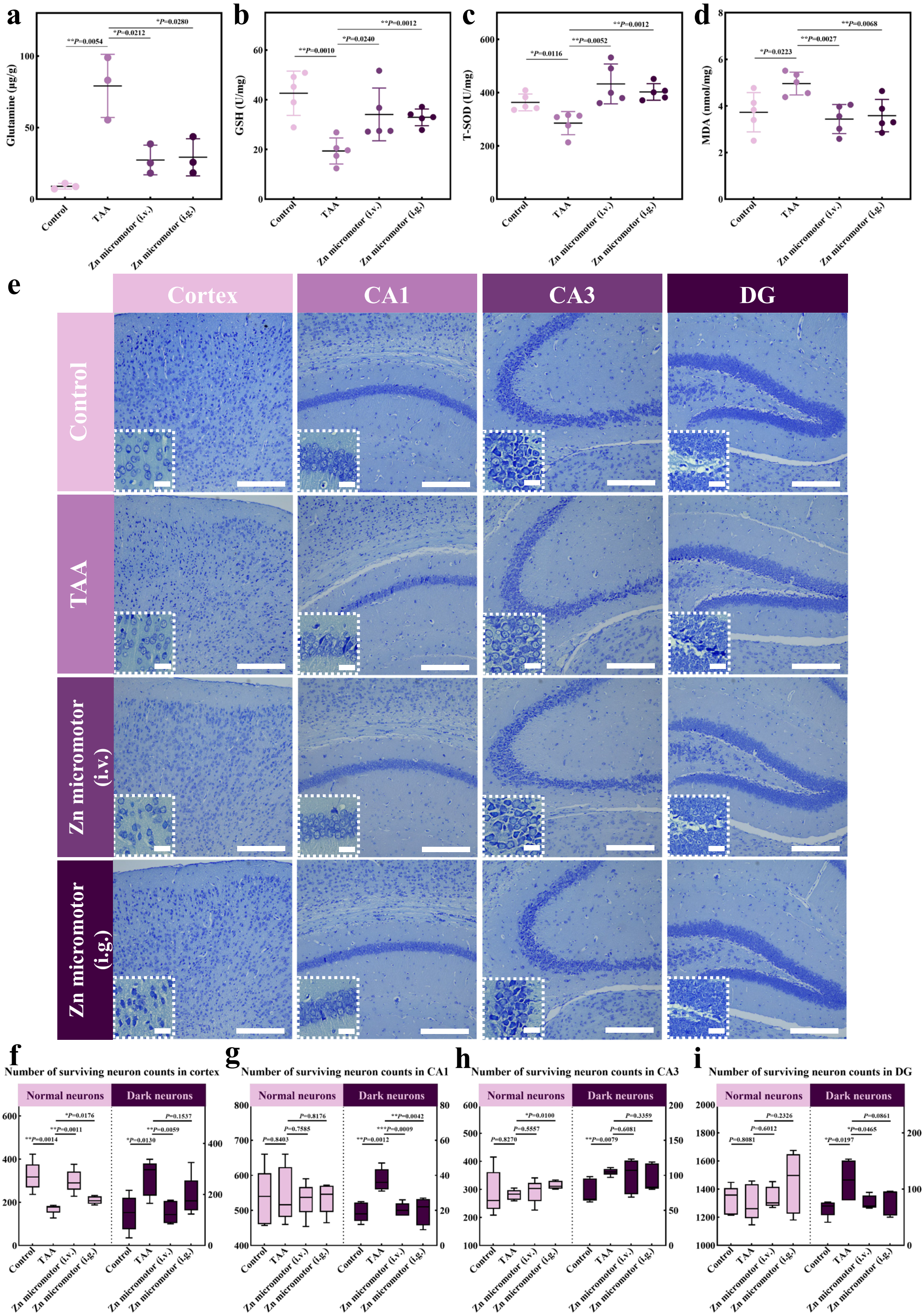

were identified as damaged neurons, often referred as dark neurons[46,47]. Neuronal necrosis, a decrease in the number of Nissl bodies, and an increase in dark neurons were observed following neuronal damage. The areas of the cerebral cortex and CA1, CA3, and dentate gyrus (DG) of hippocampus[47] were selected to count the existing neurons and dark neurons. From Fig. 8e, it was observed that the neurons in the cortex and hippocampus (CA1, CA3, DG) of the control group were arranged regularly, the Nissl bodies within the neurons were obvious and abundant, and the number of dark neurons was low. In the TAA group, the neurons in the cerebral cortex were noticeably disordered, and the morphology exhibited a certain degree of atrophy. According to statistics, compared with the control group, the number of normal neurons in the cerebral cortex in the TAA group decreased by 47.20%, and the number of dark neurons increased by 111.11% (Fig. 8f). After treatment with Zn micromotors, the arrangement of neurons in the Zn micromotor (i.v.) group were arranged more

Fig. 8 | Brain histopathological examination. a The contents of glutamine in brain tissue of each group. ($n = 3$ independent samples) **b** GSH. **c** T-SOD. **d** MDA levels, oxidative stress biomarkers in the brain ($n = 5$ independent samples). **e** Nissl staining images of cerebral cortex and hippocampus. Scale bar: 100 μm, 200 μm. **f** Nissl staining statistical analysis of neurons and dark neurons in cerebral cortex ($n = 5$ independent samples). **g** Nissl staining statistical analysis of neurons and dark neurons in CA1 area of brain and hippocampus ($n = 5$ independent samples). **h** Nissl staining statistical analysis of neurons and dark neurons in CA3 area of brain and hippocampus ($n = 5$ independent samples). **i** Nissl staining statistical analysis of neurons and dark neurons in DG area of brain and hippocampus ($n = 5$ independent samples). Results in **f**–**i** are shown as box plots (The box represents the interquartile range (IQR), with the middle line indicating the median, the top and bottom edges of the box show the upper (Q3) and lower (Q1) quartiles respectively, while the whiskers extend to the maximum and minimum values of the dataset). Data in **a**–**d** and **f**–**i** represent as mean ± S.D. *P* values were analyzed by Student's t-test (two-tailed). The asterisks (*) denote statistical significance: $^{***}p < 0.001$, $^{**}p < 0.01$, $^{*}p < 0.05$. Source data are provided as a Source Data file.

regularly, and the degree of cell atrophy was restored. Specifically, there was a 75.94% recovery in the number of normal neurons, while the count of dark neurons decreased by 51.43% relative to the TAA group. In the Zn micromotor (i.g.) group, normal neurons showed a recovery of 23.58% compared with the TAA group; however, there was no significant difference in the number of dark neurons when compared with the TAA group. It was shown that the treatment of Zn micromotors could improve neuronal damage in the cerebral cortex, and the effectiveness of intravenous injection is better than that of gastrointestinal administration.

In the hippocampal CA1 area, as shown in the Fig. 8e and g, compared with the control group, the Nissl body staining of neurons in the TAA group was lighter and the structure was fuzzy. The number of dark neurons significantly increased by 96.84%. Compared with the TAA group, the neurons in the Zn micromotor (i.v.) group were regularly arranged, and the number of dark neurons decreased by 45.45%, and the number of dark neurons in the Zn micromotor (i.g.) group decreased by 47.59%. There was no significant difference in the number of normal neurons in each group in the CA1 area. In the hippocampal CA3 area, as shown in Fig. 8e and h, the TAA group showed neuronal edema and light Nissl body staining. According to statistics, the number of dark neurons increased by 36.36%. The Zn micromotor treatment group did not significantly improve the appearance of dark neurons in this area. The hippocampal DG area, as shown in Figs. 8e and i, revealed no significant difference in the statistical number of normal neurons among the groups. There was a significant increase of 75.38% in the number of dark neurons in the TAA group compared to the control group. Compared with the TAA group, the dark neurons in Zthe n micromotor (i.v.) group and Zn micromotor (i.g.) group decreased by 33.97% and 32.06%, respectively.

The above results proved that Zn micromotor (i.v.) treatment had a certain protective effect on neurons in the cerebral cortex and a certain inhibitory effect on the production of dark neurons in the cerebral cortex and hippocampus (CA1, DG). The therapeutic effect of Zn micromotor (i.g.) treatment was slightly less effective than that of Zn micromotor (i.v.), but it also provided a protective effect on neurons in the cerebral cortex and inhibited the production of dark neurons in the hippocampal CA1 area.

Brain edema is also considered an important feature of hepatic encephalopathy. Therefore, the brain weight ratios were calculated (Fig. 7a). Three other groups of mice showed an abnormal increase in brain weight compared to the control group, and the TAA group showed an increase in brain weight ratio of 124.40%. Compared with the TAA group, the brain weight ratio of Zn micromotor (i.v.) group and the Zn micromotor (i.g.) group decreased by 31.31% and 32.25%. These results indicated that Zn micromotors improved brain edema after treatment.

Astrocytes are the only cells in the brain that can detoxify ammonia. The abnormally elevated ammonia levels in the brain lead to astrocyte edema and dysfunction[48]. Therefore, the cerebral cortex and hippocampus were immunohistochemically labeled with GFAP antibody, and the resulting immunohistochemical maps were measured with ImageJ to calculate the mean optical density value. Results as shown in Supplementary Figs. 30, 31, GFAP expression in the cortical area of the brain was significantly reduced by 43.45% in the TAA group compared to the control group. And significantly increased by 56.20% after Zn micromotor (i.v.) treatment and by 45.57% after Zn micromotor (i.g.) treatment. There was no significant difference in the average optical density between the groups in the hippocampus, indicating that GFAP expression did not change significantly. The results showed that Zn micromotor treatment could control the amount of ammonia entering the brain, thus improving the damage to astrocytes in the cerebral cortex.

Safety evaluation of Zn micromotors in vivo

As a biomaterial used in vivo, Zn micromotors should demonstrate biocompatibility. Therefore, we first monitored the length changes of Zn micromotors at different concentrations of ammonia during different time periods. The range of blood ammonia elevation in mice caused by hyperammonemia was generally lower than 200 μM. The maximum concentration of high ammonia in the body to coma will not exceed 500 μM. Therefore, we monitored the degradation degree of Zn micromotors over time in an ammonia environment of 200 μM and 500 μM, respectively. The results in Fig. 9a showed that after 1 d, compared with the initial state (0 h, 0 μM), the Zn micromotors retained 78.75% of the length in 200 μM $NH_3·H_2O$ and 75.74% of the length in 500 μM $NH_3·H_2O$, and could still maintain the motion state. After 3 d, the Zn micromotors still retained 49.53% length in 200 μM $NH_3·H_2O$ and 40.69% length in 500 μM $NH_3·H_2O$. The experimental results showed that Zn micromotors could remain stable for more than 3 d in the presence of ammonia. In conclusion, Zn micromotors can exist in aqueous ammonia solution for more than 3 d, indicating stability and therapeutic effect in pathological ammonia environment. At the same time, the result shows that Zn micromotors can be degraded and metabolized in vivo.

Then, we performed a hemolysis test on Zn micromotors. As shown in Fig. 9b and Supplementary Fig. 32, we selected different concentrations of Zn micromotors (0.25 μg/mL, 0.50 μg/mL, 1.25 μg/mL) for co-incubation with erythrocytes. The concentration of Zn micromotors used in the experiment is within this concentration range. Within 96 h, the hemolysis rate of each concentration group was still below 5%. It indicated that Zn micromotors have high hemocompatibility.

In order to investigate the interaction between Zn micromotors and other nitrogen-containing molecules, we selected the main nitrogen-containing molecules in the body, including adenosine diphosphate, adenosine monophosphate, glycine, and cysteine. After reacting with Zn micromotor for 24 h, ESI-MS was used to detect whether there were chemical changes before and after the reaction. The results are shown in Supplementary Fig. 33a–d, which shows that after 24 h of reaction with the addition of Zn micromotors, no reaction product bound to Zn was found compared to the original compound. It indicated that Zn micromotors at this dose did not readily react with other nitrogen-containing compounds in the body. It has good ammonia specificity in vivo.

For further in vivo safety evaluation, we performed blood drug concentration monitoring after Zn micromotors treatment to check whether there was excessive Zn^{2+} residue in blood. Blood concentration monitoring was performed on serum samples at 0.17 h, 0.5 h, 1 h, 2 h, 3 h, 5 h, 8 h, 10 h, 12 h, and 24 h after intravenous and oral

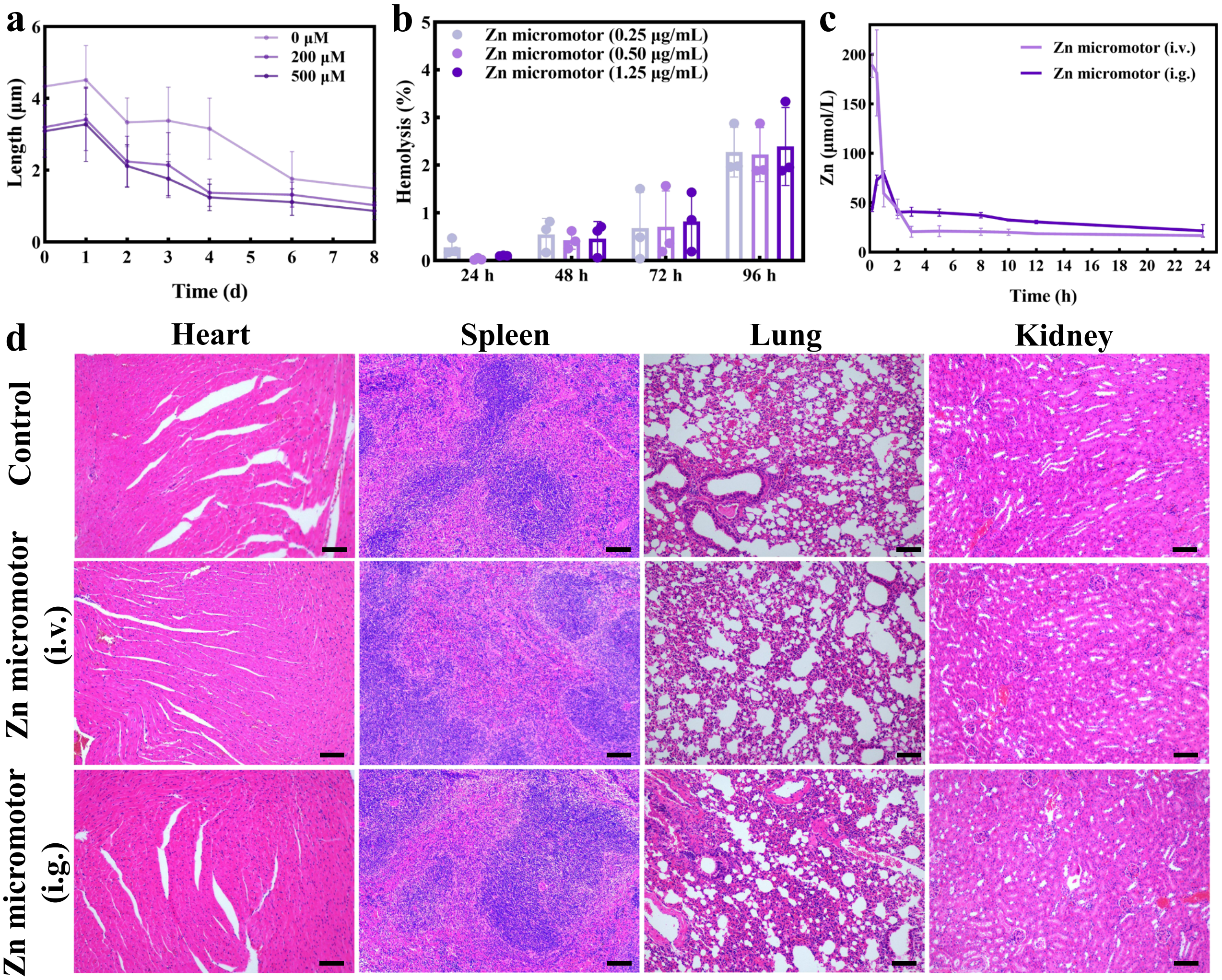

Fig. 9 | Safety evaluation of Zn micromotors in vivo. **a** Degradation degree of Zn micromotors in $NH_3{\cdot}H_2O$ ($n = 30$ independent samples). **b** Hemolysis experiment of Zn micromotors ($n = 3$ independent samples). Negative control: Red blood cells in 0.9% sodium chloride solution; Positive control: Red blood cells in water. **c** Metabolic kinetics of Zn micromotors in vivo ($n = 3$ independent samples). **d** H&E staining of main organs in each group, scale bar: 100 μm. The experiment was repeated independently three times with similar results, and a representative result is shown. Data in **a**–**c** represent as mean ± S.D. *P* values were analyzed by Student's *t*-test (two-tailed). Source data are provided as a Source Data file.

administration. Graphpad Prism 8.0.2 software was used to plot the drug-time curve, and DAS 2.0 software was used to analyze pharmacokinetic parameters using a non-compartmental model. In Fig. 9c the results showed that the peak concentration of Zn^{2+} in the blood, C_{max} (189.24 ± 12.40) μmol/L, was reached 10 min after intravenous administration. Subsequently, within 1 h, the concentration of Zn^{2+} in the blood rapidly decreased, and then Zn was slowly and stably metabolized and eliminated in the body, with a clearance rate (CL) of (0.84 ± 0.67) L/h/kg. After 1 h of oral administration, the peak concentration of Zn^{2+} in the blood was C_{max} (79.15 ± 3.12) μmol/L. Subsequently, Zn^{2+} was slowly and stably metabolized and eliminated in the body, with a clearance rate (CL) of (2.27 ± 1.15) L/h/kg. The above experiment monitored the dynamic changes of Zn micromotors, that is, the concentration of Zn^{2+} in the blood changes over time. After testing, the concentration of Zn^{2+} in the body decreased to the normal range (18.81 ± 0.77) μmol/L 12 h after intravenous administration. After 24 h of oral administration, the concentration of Zn^{2+} in the body decreased to the normal range (21.64 ± 6.42) μmol/L.

The above experiment monitored the dynamic changes of Zn micromotors in living organisms, that is, the concentration of Zn^{2+} in the blood changes over time. The experimental results showed that after treatment with Zn micromotors, the concentration of Zn^{2+} in the body gradually decreased to normal within 24 h[49]. Therefore, Zn^{2+} will not produce toxicity due to excessive accumulation in the body.

Then the main organs of mice, including the heart, spleen, lung, and kidney were taken for histological analysis. The H&E staining results are shown in Fig. 9d. Compared with the control group, no significant damage was observed to organs in the body after treatment with Zn micromotors. Cardiomyocytes were arranged neatly. The splenic-medullary junction was evident, with a dense distribution of lymphocytes. The lung alveoli were evenly distributed, and the epithelial cells were neatly arranged. The epithelial cells of renal tubules were arranged neatly and the renal corpuscles were uniform in texture. Therefore, it was proved that Zn micromotors did not cause systemic toxicity after intravenous injection and intragastric administration.

Discussion

Inspired by the autonomous motility and versatility of living organisms in nature, artificial micro/nanomotors are engineered to be applied in biomedical scenarios. However, with rapid development in this direction, moving controllability issue is beginning to emerge, or the ability to propel autonomously while ensuring precise targeting. Accurate delivery to the target site avoids accumulation in healthy tissue and unnecessary side effects. Chemotaxis of artificial micro/nanomotors emerges as an effective solution for autonomous collective navigation and in vivo targeted therapy.

To achieve the directional enrichment of artificial micro/nanomotors in vivo, we have developed an artificial micromotor navigation system. The metallic Zn micromotors are chemically actuated by complexation reaction. With ammonia as a chemical attractant, Zn micromotors can chemotactically advance in the direction of high ammonia concentration. For in vitro model, the Zn micromotors followed the ammonia concentration gradient, achieving long-distance autonomous migration toward an ammonia source. A dynamic flow environment was also provided by a microfluidic device, demonstrating the ability of Zn micromotors to move towards ammonia in a flowing fluid environment. It provided further proof for the application of Zn micromotors in vivo. For in vivo applicability, we chose the TAA-induced liver fibrosis model mice. Upon hepatocytes injury in TAA, the ability to scavenge ammonia is greatly reduced (3.05 times increased in blood ammonia concentration compared to the control group), leading to ammonia accumulation in the liver, which aggravated liver fibrosis and induces hyperammonemia. Excess ammonia penetrates the blood-brain barrier in a non-ionic form and accumulates in the brain, causing oxidative stress, neuronal necrosis and hepatic encephalopathy.

Clinical prognosis of liver fibrosis and the treatment of hepatic encephalopathy focus on reducing blood ammonia. Zn micromotors exhibit chemotaxis towards ammonia, we have designed them to target the colon (ammonia production site) and liver (ammonia metabolism site) through oral or intravenous injection, respectively. The micromotors locate and target areas of high ammonia concentration, and trap ammonia during their movement via coordination reactions, forming the complex ions $[Zn(NH_3)_1](OH)^+$ and $[Zn(NH_3)_2](OH)^+$, which could be excreted via kidney. This process further reduces the concentration of ammonia in the circulation system (42.13% – 44.59% decrease). Moreover, Zn itself can assist the liver in ammonia metabolism[50–52]. The system prevents further aggravation of liver fibrosis and reduces the deposition of collagen fibers by lowering ammonia accumulation in the liver (38.33% reduction in fibrotic area for intravenous treatment group, 31.81% reduction for oral treatment group). With minimized ammonia penetration into the brain, the number of normal neurons in the cerebral cortex experienced an increase (75.94% increase after intravenous injection and 23.58% increase after oral treatment). Behaviorally, the treatment of Zn micromotors also improved the moving dysfunction of mice. After intravenous injection of Zn micromotors, the average mice moving speed increased by 9.21 times compared with the TAA group. At the same time, it improved the cognitive function and coordination ability of mice.

In this study, we propose a generalizable chemotaxis strategy through coordination reaction. Through the interplay (complexation) between the imposed external ammonia gradient and the self-generated Zn ion gradient of the active material, long-distance and collective directional navigation is realized. Upon reaching the target position, the hybrid interface traps excess ammonia to generate complex ions, thus reshaping the local pathological microenvironment and reducing the toxicity of ammonia. Compared with the traditional clinical treatment of hyperammonemia and hepatic encephalopathy, including dialysis and perfusion, the treatment method of Zn micromotors is mild. Compared with other biomaterials, Zn micromotors can be effectively enriched by autonomous chemotaxis. With Zn, micromotors can continuously react and degrade in vivo,and they also demonstrate good biocompatibility. This adaptive system represents an intelligent chemotactic navigation therapy, providing a promising approach for green and precision therapy in the future.

Methods

Ethical Statement

Associated animal use protocols have been reviewed and approved by the Institutional Animal Care and Use Committee (IACUC) of Sun Yat-sen University (SYSU-IACUC-2022-001951). Male and female Balb/c mice (6–8 weeks) were provided by the Laboratory Animal Center of Sun Yat-sen University and were housed according to standard procedures at temperature (20–25 °C), relative humidity (40–60%), a 12 h light/dark cycle and in a specific pathogen-free environment. Food and water were freely available for five days prior to the start of the experiment to allow for environmental acclimatization.

Materials

Polycarbonate film (PC film) was purchased from Whatman (Shanghai, China). Boric acid (H_3BO_3) and aqueous ammonia ($NH_3{\cdot}H_2O$) were purchased from Macklin (Shanghai, China). Zn sulfate heptahydrate ($ZnSO_4{\cdot}7H_2O$) was purchased from Aladdin (Shanghai, China). Ethanol and dichloromethane (CH_2Cl_2) were purchased from Guangzhou Chemical Reagent Factory (Guangzhou, China). Thioacetamide (TAA) was purchased from MeilunBio (Dalian, China). GFAP Rabbit Polyclonal Antibody (16825-1-AP) was purchased from Proteintech Group (Wuhan, China). Blood Ammonia Content Assay Kit was purchased from Beijing Solarbio Science & Technology Co.,Ltd. (Beijing, China). Alanine Aminotransferase (ALT) assay kit, Aspartate Aminotransferase (AST) assay kit, and Albumin (ALB) assay kit were purchased from Rayto (Shenzhen, China). Total bilirubin assay kit was purchased from Changchun Huili Biotech Co., ltd (Changchun, China). Zn Assay Kit and Glutathione Peroxidase (GSH-PX) assay kit were purchased from Nanjing Jiancheng Bioengineering Institute (Nanjing, China). Total Superoxide Dismutase (T-SOD) Assay Kit and Malondialdehyde (MDA) assay kit were purchased from Servicebio (Wuhan, China).

Instruments

SEM and EDX images were obtained on a Cold Field Emission Scanning Electron Microscope (S-4800, HITACHI). The particle motion was obtained on fluorescence microscopy (Ti2-A, Nikon). Mass spectrum was measured by Tims-TOF MS (UltiMate3000-timsTOF, Bruker). Blood biochemistry was measured by a fully automated biochemical analyzer (Chemray 240, Rayto). The biochemical antioxidant indicators were measured by a microplate reader (Epoch, BioTek). The sliced images were obtained on a standing optical microscope (NIKON ECLIPSE E100, Nikon). In vivo imaging was measured by a small animal live imaging system (IVIS SPECTRUM, PerkinElmer).

All statistical analyses were conducted using GraphPad Prism 8.0, Origin 8.5, Microsoft Office Excel 2019, and Image J. Chemotaxis and Migration Tool software was used to analyze particle tracking. Tracker software was used to analysis was used to analysis animal motion tracking. The slice data were analyzed using CaseViewer 2.4.0. Particle motion simulation was conducted using the multi-physics field finite element analysis software COMSOL 6.2. Living image software was used to analyze fluorescent images.

Fabrication of Zn micromotors

Zn micromotors were fabricated by electrochemical deposition using the membrane plate method. The three-electrode system was selected, and the corresponding three electrodes were a working electrode (copper electrodeposition support, 13 mm PEEK), a reference electrode (Ag/AgCl), and a counter electrode (platinum wire). Polycarbonate membrane is used for formwork. First, a 100 nm thick gold layer was evaporated on one side of the polycarbonate film using an electron beam evaporation wave test DE400 for conductivity and to close the single-sided film aperture. The polycarbonate film (gold layer) was covered on the working electrode for electrochemical deposition using an electrochemical workstation. At room temperature, a mixed solution of 0.2 M $ZnSO_4{\cdot}7H_2O$ and 0.1 M boric acid was used for electrodeposition at a constant voltage of −1.23 V for 15 min. After the preparation, the gold layer on the membrane surface was removed by physical friction, and then the polycarbonate membrane template was dissolved with dichloromethane. The Zn micromotors were dispersed in water for storage.

Characterization of Zn micromotors

Zn micromotors were dispersed with ethanol on silicon wafers, dried and characterized by scanning electron microscopy (SEM) and energy dispersive X-ray spectroscopy (EDX) (Hitachi, regulus 8230). The movement of Zn micromotors in water were recorded using Nikon inverted microscope (Nikon, Ti2-A) and NIS-Element Viewer software.

Chemotaxis experiment

$NH_3 \cdot H_2O$ chemotaxis experiments with Z-shaped glass channel for Zn micromotors. The specific parameters of this channel were shown in Supplementary Fig. 9. The volume of DI water added to the channel in each experiment is 500 µL, and the volume of $NH_3 \cdot H_2O$ added to the B chamber is 10 µL.

COMSOL multiphysics calculation

The chemotactic movement of the Zn tube micromotor comes from a chemical reaction:

$$2Zn + 4H_2O + 3NH_3 \rightarrow [Zn(NH_3)_1](OH)_2 + [Zn(NH_3)_2(OH)_2 + 2H_2 \quad (1)$$

A constant flux of $[Zn(NH_3)_1](OH)^+$, $[Zn(NH_3)_2](OH)^+$, and OH^- is set on the surface of the Zn tube micromotor. The initial concentration in the physical field set by the model is 0. The water flow velocity at the boundary of the Zn tube micromotor is 0. The outflow of $[Zn(NH_3)_1](OH)^+$, $[Zn(NH_3)_2](OH)^+$, and OH^- on the surface of the micromotor is affected by ion diffusion, convection, and migration.

The physical field of diffusion is controlled by the following equation, which follows the conservation of matter:

$$\frac{\partial c_i}{\partial t} + \nabla \cdot J_i + u \cdot \nabla c_i = R_i \quad (2)$$

$$J_i = -D_i \cdot \nabla c_i - z_i u_{m,i} \cdot F c_i \cdot \nabla V \quad (3)$$

Where, t is the time, J_i is the energy diffusion coefficient of species i, μ is the fluid velocity, c_i is the concentration of species i, R_i is the flux of species i, D_i is the diffusion coefficient of species i, z_i is the charge of species i, μ_m is the viscosity, F is the volume force, and V is the volume.

The current passing through any closed surface in a constant electric field is 0.

The potential in Eq. 1 is calculated using the Poisson equation (φ):

$$-\varepsilon_0 \varepsilon_r \boldsymbol{\nabla}^2 \varphi = \rho_e = F\left(z_+ c_+ + z_{-} c_{-}\right) \quad (4)$$

where ε_0 is the permittivity of the vacuum, and ε_r is the relative permittivity of the fluid media, ρ_e is the volumetric charge density, z_+ and z_- are the charges of the cations and the anions, c_+ and c_- are the concentrations of the cations and the anions.

The inertial effect is neglected because of a very small Reynolds number. Thus, the flow field is governed by the Stokes equations,

$$-\nabla p + \mu \nabla^2 \boldsymbol{u} = 0 \quad (5)$$

and the continuity equation for the incompressible fluid,

$$\nabla \cdot \boldsymbol{u} = 0 \quad (6)$$

where p is the pressure, $\boldsymbol{u}$ is the fluid velocity vector. The initial values of the flow velocity and the pressure are all zero.

Cell lines

AML12 cell complete culture medium (IMMOCELL, IM-M054-B) was used to cultivate AML-12 (Mouse liver cells) cells (IMMOCELL, IM-M054-A) that were purchased from Xiamen Immocell Biotechnology Co., Ltd. DMEM complete medium (GIBCO, C11965500BT) was used to cultivate HT22 (Mouse hippocampal neurons) cells (CL-0697) that were purchased from Wuhan Pricella Biotechnology Co., Ltd. The cells were incubated at 37 °C in a humidified incubator with 5% CO_2.

Animal experiments

After five days of adaptation, refer to the experimental protocol. Twenty mice were randomly divided into the following four groups: (1) The control group was given 0.9% (w/v) normal saline (5 ml/kg, i.p., 3 times per week for 6 weeks); (2) Thioacetamide (TAA) model group (100 mg/kg, i.p., 3 times per week for 6 weeks); (3) Zn micromotors (i.v.) group (TAA 100 mg/kg, i.p., 3 times per week for 6 weeks; Zn micromotors, 10 µL/g, i.v., was given from the second week, 3 times per week for 8 weeks); (4) Zn micromotors (i.g.) group (TAA 100 mg/kg, i.p., 3 times per week for 6 weeks; Zn micromotors, 10 µL/g, i.g., was given from the second week, 2 times per week for 8 weeks) was given from the second week. Body weight was recorded before each administration. Mouse movement tracking was performed after each administration in the last week. Two hours after the last administration, the mice were euthanized, and blood samples were collected. Liver and brain were harvested, weighed, and a portion used to prepare tissue homogenate, and the remainder preserved for histopathological examination.

Balance beam test

The beam of the balance device is 1 m long and 6 mm wide on the plane surface. A black box is placed at the end of the beam as the completion point. The nesting materials from the original home cage were put into the black box to attract the test mice. A lamp was placed above the starting point as a stimulus that disgusted the mouse. A buffer belt is set under the beam to cushion the falling mice. Before the formal test, the mice should be familiarized with the experimental environment, and the animals should be trained. Starting from the thicker beam, gradually reduce the width, and let the mice walk many times until skilled. In the formal test, the starting point is at 0 cm and the end point is at 80 cm. Record the test process through the camera.

Data recording and analysis, record the passing time, falling times, and posture adjustment of each animal. 0 points, the mouse cannot grasp the beam or falls directly on the beam; 1 point, can grasp the beam or sit on the beam, can not move, but can stay for 1 min; 2 points, can keep balance on the beam, cannot cross the beam, but can stay for 1 min; 3 points, can walk from one end of the beam to the other, but there are footsteps; 4 points, can walk freely from one end to the other.

Y-maze spontaneous alternation experiment

The device consists of three equal-length arms (30 cm × 6 cm × 15 cm), and the included angle between each arm is 120°. The mice are placed at the end of any arm of the Y-maze and allowed to explore freely. The total number of entries recorded by the camera is 20 times; Among them, one continuous entry into all three arms of the Y maze is recorded as an alternation. Spontaneous alternation behavior score = Total number of alternations/(the total number of entries − 2).

Body weight change

The formula for calculating the percentage change in mouse weight is: (Body weight of the next day - Body weight of the previous day) × 100%/ Body weight of the previous day.

Measurement of liver, brain body weight index

The liver and brain were weighed and recorded immediately after removal.

The formula of liver body weight index (LBWI) and brain body weight index (BBWI) are: LBWI = (liver weight/body weight) and BBWI= (brain weight/body weight), respectively.

Behavioral observation

In a quiet environment, the mice were put into a round glass container at the bottom of the open field box, and the movie was taken and timed for 5 min at the same time. The voluntary movements of the mice were observed and recorded, the trajectories were plotted using the Tracker software, and the speeds of movement were calculated.

Biochemical assay

Blood was collected from the orbits and allowed to stand at room temperature (25 °C) for 1 h, then centrifuged at 750 × *g* for 15 min at 4 °C. Transfer the supernatant, i.e. serum, to the corresponding labeled sample tube for storage, and store the serum at −80 °C after collection, waiting for subsequent detection. The contents of blood ammonia, alanine aminotransferase (ALT), aspartate aminotransferase (AST), albumin (ALB), total bilirubin, and Zn in serum were determined according to the instructions of the biochemical detection kit. Take an appropriate amount of liver and cerebral cortex tissue to prepare tissue homogenate, and determine the contents of glutathione peroxidase (GSH-Px), total superoxide dismutase (T-SOD), and malondialdehyde (MDA) in tissue homogenate according to the instructions of the biochemical detection kit.

Histopathological examination

The liver and brain of mice were taken, washed with PBS (pH 7.4), and the tissues were fixed in 4% paraformaldehyde (PFA). Then they were dehydrated and embedded in paraffin, sliced at approximately 5 µm thickness using a pathology slicer (Leica Biosystems, Germany), and the slices were fixed onto microscope slides.

H&E staining analysis: Each group of liver and brain tissue sections was stained with haematoxylin and eosin (H&E). After staining, tissue images of the liver and brain were taken under a microscope. The pathological changes in the tissues were observed.

Sirius red staining analysis: Liver tissues of each group were stained with Sirius red staining solution, and after staining, images of liver tissues were taken using a microscope, and the images were processed using ImageJ software to statistically measure the area of Sirius red collagen fibers, which was used to observe the degree of liver fibrosis in mice.

Nissl staining analysis: Brain tissues of each group were stained with Nissl staining solution. After staining, the brain tissue images were taken using a microscope, and the number of normal neurons and dark neurons in the cerebral cortex and hippocampus (CA1, CA3, DG) were counted using ImageJ software. It was used to observe the neuronal damage in the cerebral cortex and hippocampus of mice.

Immunohistochemistry analysis

The basic procedure is to repair the antigen with the repair solution. Sections were incubated in 3% H_2O_2 solution for 20 min at room temperature to block endogenous peroxidase. After blocking with 3% bovine serum albumin BSA for 30 min, GFAP rabbit polyclonal antibody (16825-1-AP, Proteintech) (1:5000) was added and incubated overnight at 4 °C. The next day, the tissue was labeled with horseradish peroxidase (HRP) (GB23303, Servicebio) (1:200) secondary antibody and incubated for 1 h at room temperature. Brain tissue images were taken using a microscope after DAB (3,3′-diaminobenzidine) color development, and semi-quantitative statistics were performed on the sections using ImageJ software, using the average optical density values expressed for the observation. The extent of damage to astrocytes in the cerebral cortex and hippocampus (CA1, CA3, DG) was observed.

Statistical analysis

Data in this paper were statistically analysed using GraphPad Prism 8.0 (GraphPad Software, San Diego, CA, USA) and Origin 8.5 (OriginLab, Northampton, Massachusetts, USA). Values are expressed as mean ± standard deviation (SD). Each independent experiment had at least 5 sample replicates, and comparisons between experimental groups were statistically analyzed using the *t*-test. $p < 0.05$ was considered a statistically significant difference.

Reporting summary

Further information on research design is available in Nature Portfolio Reporting Summary linked to this article.

Data availability

The source data generated in this study are provided in the Supplementary Information/Source Data file. The full image dataset is available from the corresponding author upon request. Source data are provided for Figs. 2–9 and Supplementary Figs. 5, 7, 8, 12, 13, 15–23, 26-28, 31, and 33 in the associated source data file available on Figshare: https://doi.org/10.6084/m9.figshare.28776902.

References

1. Savy, N. et al. Acute pediatric hyperammonemia: current diagnosis and management strategies. *Hepat. Med.-Evid. Res.* **10**, 105–115 (2018).
2. Rangroo Thrane, V. et al. Ammonia triggers neuronal disinhibition and seizures by impairing astrocyte potassium buffering. *Nat. Med.* **19**, 1643–1648 (2013).
3. Häussinger, D. Hepatocyte heterogeneity in glutamine and ammonia metabolism and the role of an intercellular glutamine cycle during ureogenesis in perfused rat liver. *Eur. J. Biochem.* **133**, 269–275 (1983).
4. Keiding, S., Munk, O., Roelsgaard, K., Bender, D. & Bass, L. Positron emission tomography of hepatic first-pass metabolism of ammonia in pig. *Eur. J. Nucl. Med. Mol.* **28**, 1770–1775 (2001).
5. Wierling, C. Bridging the gap between metabolic liver processes and functional tissue structure by integrated spatiotemporal modeling applied to hepatic ammonia detoxification. *J. Gastroen. Hepatol.* **60**, 1823–1825 (2014).
6. Hakvoort, T. B. et al. Pivotal role of glutamine synthetase in ammonia detoxification. *J. Hepatol.* **65**, 281–293 (2017).
7. Jalan, R. et al. Ammonia produces pathological changes in human hepatic stellate cells and is a target for the therapy of portal hypertension. *J. Hepatol.* **64**, 823–833 (2016).
8. Lu, K. et al. Hepatic encephalopathy is linked to alterations of autophagic flux in astrocytes. *EBioMedicine* **48**, 539–553 (2019).
9. Qiu, J. et al. Hyperammonemia-mediated autophagy in skeletal muscle contributes to the sarcopenia of cirrhosis. *Am. J. Physiol. -Endocrinol. Metab.* **303**, E983–E993 (2012).
10. Häussinger, D. et al. Hepatic encephalopathy. *Nat. Rev. Dis. Prim.* **8**, 43 (2022).
11. Jepsen, P., Ott, P., Andersen, P. K., Sørensen, H. T. & Vilstrup, H. Clinical course of alcoholic liver cirrhosis: a Danish population-based cohort study. *J. Hepatol.* **51**, 1675–1682 (2010).
12. Meijer, A. J., Lamers, W. H. & Chamuleau, R. Nitrogen metabolism and ornithine cycle function. *Physiol. Rev.* **70**, 701–748 (1990).
13. Vilstrup, H. et al. Hepatic encephalopathy in chronic liver disease: 2014 Practice Guideline by the American Association for the Study of Liver Diseases and the European Association for the Study of the Liver. *J. Hepatol.* **60**, 715–735 (2014).
14. Arguedas, M. R., DeLawrence, T. G. & McGuire, B. M. Influence of hepatic encephalopathy on health-related quality of life in patients with cirrhosis. *Dig. Dis. Sci.* **48**, 1622–1626 (2003).
15. Prakash, R. & Mullen, K. D. Mechanisms, diagnosis and management of hepatic encephalopathy. *Nat. Rev. Gastroenterol. Hepatol.* **7**, 515–525 (2010).
16. Montagnese, S. et al. A pilot study of golexanolone, a new GABA-A receptor-modulating steroid antagonist, in patients with covert hepatic encephalopathy. *J. Hepatol.* **75**, 98–107 (2021).

17. Ott, P. & Vilstrup, H. Cerebral effects of ammonia in liver disease: current hypotheses. *Metab. Brain Dis.* **29**, 901–911 (2014).
18. Cooper, A. J. The role of glutamine synthetase and glutamate dehydrogenase in cerebral ammonia homeostasis. *Neurochem* **37**, 2439–2455 (2012).
19. Aldridge, D. R., Tranah, E. J. & Shawcross, D. L. Pathogenesis of hepatic encephalopathy: role of ammonia and systemic inflammation. *J. Clin. Exp. Hepatol.* **5**, S7–S20 (2015).
20. Abbott, N. J., Rönnbäck, L. & Hansson, E. Astrocyte–endothelial interactions at the blood–brain barrier. *Nat. Rev. Neurosci.* **7**, 41–53 (2006).
21. Butterworth, R. F., Girard, G. & Giguère, J. F. Regional differences in the capacity for ammonia removal by brain following portocaval anastomosis. *J. Neurochem.* **51**, 486–490 (1988).
22. Suraweera, D., Sundaram, V. & Saab, S. Evaluation and management of hepatic encephalopathy: current status and future directions. *Gut Liver* **10**, 509 (2016).
23. Felipo, V. Hepatic encephalopathy: effects of liver failure on brain function. *Nat. Rev. Neurosci.* **14**, 851–858 (2013).
24. Angelova, P. R. et al. Hyperammonaemia induces mitochondrial dysfunction and neuronal cell death. *JHEP Rep.* **4**, 100510 (2022).
25. Adler, J. Chemoreceptors in Bacteria: Studies of chemotaxis reveal systems that detect attractants independently of their metabolism. *Science* **166**, 1588–1597 (1969).
26. Frankel, N. W. et al. Adaptability of non-genetic diversity in bacterial chemotaxis. *Elife* **3**, e03526 (2014).
27. Iijima, M., Huang, Y. E. & Devreotes, P. Temporal and spatial regulation of chemotaxis. *Dev. Cell* **3**, 469–478 (2002).
28. Bloes, D. A., Kretschmer, D. & Peschel, A. Enemy attraction: bacterial agonists for leukocyte chemotaxis receptors. *Nat. Rev. Microbiol.* **13**, 95–104 (2015).
29. Wong, C. H., Heit, B. & Kubes, P. Molecular regulators of leucocyte chemotaxis during inflammation. *Cardiovasc. Res.* **86**, 183–191 (2010).
30. Tang, S. et al. Enzyme-powered Janus platelet cell robots for active and targeted drug delivery. *Sci. Robot.* **5**, eaba6137 (2020).
31. Colin, R., Drescher, K. & Sourjik, V. Chemotactic behaviour of Escherichia coli at high cell density. *Nat. Commun.* **10**, 5329 (2019).
32. Arqué, X. et al. Intrinsic enzymatic properties modulate the self-propulsion of micromotors. *Nat. Commun.* **10**, 2826 (2019).
33. Joseph, A. et al. Chemotactic synthetic vesicles: Design and applications in blood-brain barrier crossing. *Sci. Adv.* **3**, e1700362 (2017).
34. Somasundar, A. et al. Positive and negative chemotaxis of enzyme-coated liposome motors. *Nat. Nanotechnol.* **14**, 1129–1134 (2019).
35. Wang, W. et al. Acoustic propulsion of nanorod motors inside living cells. *Angew. Chem. Int. Ed.* **53**, 3201–3204 (2014).
36. Dai, B. et al. Programmable artificial phototactic microswimmer. *Nat. Nanotechnol.* **11**, 1087–1092 (2016).
37. Loget, G. & Kuhn, A. Electric field-induced chemical locomotion of conducting objects. *Nat. Commun.* **2**, 535 (2011).
38. Tottori, S. et al. Magnetic helical micromachines: fabrication, controlled swimming, and cargo transport. *Adv. Mater.* **24**, 811–816 (2012).
39. Sengupta, S., Ibele, M. E. & Sen, A. Die phantastische Reise: Nanoroboter mit Eigenantrieb. *Angew. Chem. Int. Ed.* **124**, 8560–8571 (2012).
40. Frank, B. D. et al. Reversible morphology-resolved chemotactic actuation and motion of Janus emulsion droplets. *Nat. Commun.* **13**, 2562 (2022).
41. de Ávila, B. E.-F. et al. Micromotor-enabled active drug delivery for in vivo treatment of stomach infection. *Nat. Commun.* **8**, 272 (2017).
42. Wu, C. et al. Ion-exchange enabled synthetic swarm. *Nat. Nanotechnol.* **16**, 288–295 (2021).
43. Feng, Y. et al. Directed neural stem cells differentiation via signal communication with Ni–Zn micromotors. *Adv. Mater.* **35**, 2301736 (2023).
44. Liu, A. et al. Advances in cirrhosis: optimizing the management of hepatic encephalopathy. *World J. Hepatol.* **7**, 2871 (2015).
45. Lemberg, A. & Fernández, M. A. Hepatic encephalopathy, ammonia, glutamate, glutamine and oxidative stress. *Ann. Hepatol.* **8**, 95–102 (2009).
46. Ishida, K. et al. Argyrophilic dark neurons represent various states of neuronal damage in brain insults: some come to die and others survive. *Neuroscience* **125**, 633–644 (2004).
47. Poirier, J., Čapek, R. & De Koninck, Y. Differential progression of Dark Neuron and Fluoro-Jade labelling in the rat hippocampus following pilocarpine-induced status epilepticus. *Neuroscience* **97**, 59–68 (2000).
48. Sepehrinezhad, A., Zarifkar, A., Namvar, G., Shahbazi, A. & Williams, R. Astrocyte swelling in hepatic encephalopathy: molecular perspective of cytotoxic edema. *Metab. Brain Dis.* **35**, 559–578 (2020).
49. Katayama, K. et al. Effects of zinc acetate on serum zinc concentrations in chronic liver diseases: a multicenter, double-blind, randomized, placebo-controlled trial and a dose adjustment trial. *Biol. Trace Elem. Res.* **195**, 71–81 (2020).
50. Stamoulis, I., Kouraklis, G. & Theocharis, S. Zinc and the liver: an active interaction. *Dig. Dis. Sci.* **52**, 1595–1612 (2007).
51. Katayama, K. et al. The prevalence and implication of zinc deficiency in patients with chronic liver disease. *J., Clin. Med.* **10**, 437 (2018).
52. Marchesini, G., Fabbri, A., Bianchi, G., Brizi, M. & Zoli, M. Zinc supplementation and amino acid-nitrogen metabolism in patients with advanced cirrhosis. *J. Hepatol.* **23**, 1084–1092 (1996).

Acknowledgements

This work was supported by the National Natural Science Foundation of China (Grant No. 22375224, F.P.; 51973241, F.P.; 22175083, Y.T.), Guangdong Provincial Science Foundation for Distinguished Young Scholars (Grant no. 2018B030306007, F.P.), and National Key Research and Development Program (2022YFA1206900, Y.T.).

Author contributions

Y.T. and F.P. conceptualized the study and acquired funds. Y.F., C.G., B.C., and M.D. conducted experiments. Y.F. and D.D. carried out data analyses. Q.L. and J.R. provided experimental expertise. X.P. performed COMSOL multiphysical field simulations. Y.F. and C.G. wrote and edited the manuscript. D.A.W. reviewed the manuscript.

Competing interests

The authors declare no competing interests.

Additional information

Supplementary information The online version contains supplementary material available at https://doi.org/10.1038/s41467-025-59650-0.

Correspondence and requests for materials should be addressed to Fei Peng.

Peer review information *Nature Communications* thanks Joy Jiang and the other anonymous reviewer(s) for their contribution to the peer review of this work. A peer review file is available.